Onset of absolutely unstable behaviour in the Stokes layer: A Floquet approach to the Briggs method

Alexander Pretty [1], Christopher Davies [2], and Christian Thomas [3]†

[1]School of Mathematics, Cardiff University, Cardiff, CF24 4AG, UK

[2]School of Engineering, University of Leicester, University Road, Leicester, LE1 7RH, UK

[3]Department of Mathematics and Statistics, Macquarie University, New South Wales, 2109, Australia

For steady flows, the Briggs (1964) method is a well established approach for classifying disturbances as either convectively or absolutely unstable. Here, the framework of the Briggs method is adapted to temporally periodic flows, with Floquet theory utilised to account for the time-periodicity of the Stokes layer. As a consequence of the antiperiodicity of the flow, symmetry constraints are established that are used to describe the pointwise evolution of the disturbance, with the behaviour governed by harmonic and subharmonics modes. On coupling the symmetry constraints with a cusp map analysis, multiple harmonic and subharmonic cusps are found for each Reynolds number of the flow. Therefore, linear disturbances experience subharmonic growth about fixed spatial locations. Moreover, the growth-rate associated with the pointwise development of the disturbance matches the growth-rate of the disturbance maximum. Thus, the onset of the Floquet instability (Blennerhassett & Bassom 2002) coincides with the onset of absolutely unstable behaviour. Stability characteristics are consistent with the spatiotemporal disturbance development of the family-tree structure that has hitherto only been observed numerically via simulations of the linearised Navier–Stokes equations (Thomas *et al.* 2014; Ramage *et al.* 2020).

1. Introduction

The Stokes layer is the flow established by the sinusoidal motion of an infinitely long bounding flat plate beneath an otherwise stationary body of fluid. This unsteady flow yields one of the few known exact solutions to the Navier–Stokes equations, and so is the archetype model for investigating stability behaviour in temporally periodic flows. Given the periodicity of the underlying basic state, the stability problem naturally lends itself to Floquet analysis, whereby the net growth (or decay) of linear disturbances is determined over each full cycle of wall oscillation.

The Floquet approach accounts for the periodicity of the unsteady flow by assuming that disturbances are decomposed into modes with a time-dependency of the form $\exp(\mu t)p(t)$, where p is a time-periodic function with the same period as the basic state. The net growth of the disturbance is then encompassed in the real part of the Floquet exponent μ. Perturbation equations are derived from the Navier–Stokes equations in a manner analogous to the derivation of the Orr–Sommerfeld equation (that governs the stability of steady flows).

† Email address for correspondence: christian.thomas@mq.edu.au

1.1. *General background*

Floquet theory was first formulated for the Stokes layer by Hall (1978), who showed that the flow is linearly stable for Reynolds numbers $Re < 160$ – a formal definition for the Reynolds number Re is given below in equation (2.3). Following the advancement of computational technology, Blennerhassett & Bassom (2002) extended the Floquet analysis to significantly larger values of Re, wherein a section of the neutral stability curve was traced and it was determined that linearly unstable behaviour emerges for the critical Reynolds number $Re_c = 707.84$. Equivalent formulations were subsequently used to investigate the linear stability of related flows, such as the finite Stokes layer in channels and pipes (Blennerhassett & Bassom 2006; Thomas *et al.* 2011, 2012).

Informed by the results of these earlier studies, Thomas *et al.* (2014) carried out direct numerical simulations (DNS) of the linearised Navier–Stokes equations to explore the impulse response of disturbances in the semi-infinite Stokes layer. Numerical simulations revealed an intriguing spatiotemporal formation that was described as a *family-tree* structure, which involves the successive birthing of distinct wavepackets. Moreover, it was demonstrated that DNS calculations were in excellent agreement with the Floquet stability analysis, despite computational restrictions limiting DNS to the first three periods of wall motion.

Although agreement between linear stability analysis and DNS was demonstrated, experiments on the Stokes layer generally observe unstable behaviour and transition to turbulence for Reynolds numbers $Re < 300$ (Akhaven *et al.* 1991; Clamen & Minton 1977; Eckmann & Grotberg 1991; Hino *et al.* 1976), which is significantly lower than the Floquet predictions (Blennerhassett & Bassom 2002). In an attempt to address the significant differences between theory and experiments, it was noted by Thomas *et al.* (2015) that many experiments report some noise associated with the mechanical oscillation of the bounding plate. Naturally, it is difficult to retroactively determine the level of noise in experiments, but many experimentalists quote a noise amplitude of 1% of the fundamental oscillation. Based on this observation, Thomas *et al.* (2015) undertook a stability investigation of the Stokes layer subject to a low-amplitude, high-frequency harmonic. It was shown that the introduction of this form of modulation brought about a dramatic destabilisation of the flow, bringing the critical Reynolds number Re_c for unstable behaviour in line with experimental observations. While the form of these high-frequency harmonics is not particularly comparable to the supposedly random noise observed in experiments, the considerable reduction in Re_c suggests that the presence of noise can have a significant effect on the stability of the flow.

This investigation follows the recent work by Ramage *et al.* (2020) in which disturbance development was successfully simulated for 20 periods of wall motion for both the classical Stokes layer and several cases where the basic state was modified via a high-frequency, low-amplitude harmonic. The longer time numerical simulations suggest that the Stokes layer is subject to an absolute form rather than a convective form of instability. Convective instability describes an unstable disturbance that propagates along one direction only, while absolute instability is characterised by growth at every spatial location.

1.2. *Key features of the disturbance development*

In order to fully contextualise the present investigation, we describe the key observations of Ramage *et al.* (2020) that will be explored further herein.

Figure 1 is a reproduction of figure 3 of Ramage *et al.* (2020) and displays the impulse response of the linear disturbance in the Stokes layer at the Reynolds number $Re = 750$. Contours are based on the logarithm of the absolute value of the wall vorticity
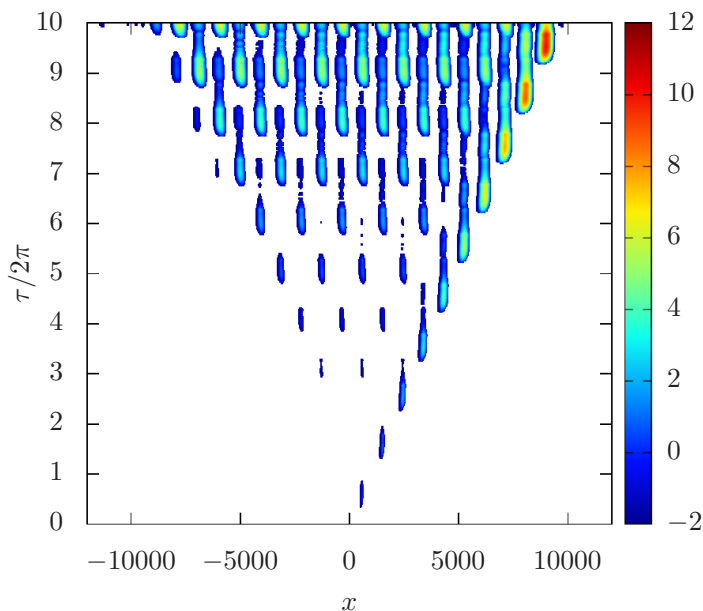
FIGURE 1. Reproduction of figure 3 from Ramage *et al.* (2020). Spatiotemporal contour plot of the linear disturbance in the Stokes layer with $Re = 750$. Contours are based on the logarithm of the absolute value of the wall vorticity perturbation.

perturbation. This plot is included here to illustrate the spatiotemporal development of the family-tree structure, first reported in Thomas *et al.* (2014), and highlight the key features of the disturbance evolution. For details on the generation of this plot, the interested reader is directed to Ramage *et al.* (2020). Here it is sufficient to state that the respective contours indicate the magnitude of the disturbance as a function of the streamwise x-direction (in which the plate oscillates) and the non-dimensional time $\tau/2\pi$ (the number of plate oscillations).

At time $\tau = 0$, the initial impulse excites a disturbance wavepacket that convects to the right. This initial wavepacket is called the *mother* wavepacket. Within each period of the wall oscillation, two *daughter* wavepackets are birthed that propagate to the left and right of the original mother wavepacket. (In the early stages of the disturbance evolution, these particular wavepackets develop at magnitudes below the low-amplitude cutoff and do not appear in the contour plot depicted in figure 1. However, they do become more obvious at later times, when the disturbance achieves larger amplitudes.) The daughter wavepackets then birth *granddaughter* wavepackets and so on, giving rise to the so-called family-tree structure shown in figure 1.

It is immediately obvious from figure 1 that the disturbance maximum convects along those wavepackets located on the right-hand side of the illustration. Moreover, the growth-rate associated with the disturbance maximum was found by Ramage *et al.* (2020) to match the growth-rate determined via Floquet stability theory (Blennerhassett & Bassom 2002).

Pointwise growth of the disturbance is then observed by selecting a single streamwise x-location and tracing the disturbance development over time, i.e. a vertical line in figure 1.

Clearly the magnitude of the disturbance, about fixed spatial positions, increases with increasing time. Though it is not evident from this plot alone, it was reported in Ramage *et al.* (2020) that the growth-rate associated with a fixed streamwise x-location is equal to (or at least remarkably close to) the growth-rate of the disturbance maximum, for all Reynolds numbers modelled. This suggests that the Stokes layer is subject to absolutely unstable behaviour, for which the onset coincides with the critical Reynolds number $Re_c = 707.84$ for linear instability (Blennerhassett & Bassom 2002).

A second observation, drawn by Ramage *et al.* (2020), is the staggered structure of the wavepacket formations. With the passing of each period of wall motion (i.e. time $\tau/2\pi$ is increased by one), the location of each wavepacket is shifted horizontally along the streamwise x-direction, before returning to their original locations during the next cycle. Thus, at fixed spatial locations, the disturbance structure reasserts itself every two cycles of wall motion. Hence, pointwise evolution is characterised by a *subharmonic* temporal growth, with a periodicity that is twice that of the basic state.

Ramage *et al.* (2020) also reported that the spacing Λ between the respective mother and daughter wavepackets is fixed and related to the Reynolds number Re. Moreover, due to the staggered nature of the family-tree formation, the distance between two adjacent wavepackets of commensurate size is twice the wavepacket spacing Λ. Thus, the family-tree structure has a spatial periodicity of 2Λ.

1.3. *Paper objective*

Although the numerical investigation by Ramage *et al.* (2020) strongly suggests that linear disturbances in the Stokes layer are absolutely unstable for Reynolds numbers $Re \geqslant Re_c$, the existence of such behaviour can only be confirmed and understood by undertaking a full theoretical study. This is achieved using a modified form of the Briggs (1964) method, based on the formulation of Brevdo & Bridges (1997).

The Briggs method for locating absolutely unstable behaviour is well established for steady flows, such as that on a rotating disc (Lingwood 1995, 1997), while Pier (2003) and Hwang *et al.* (2013) have coupled this approach with Floquet theory to study secondary instabilities on a rotating disc and in a two-dimensional wake, respectively. However, application of these routines to temporally periodic flows has not, to the authors knowledge, been attempted previously. It will be demonstrated that this analysis provides confirmation of the disturbance behaviour reported in Ramage *et al.* (2020). Moreover, we will:

  (i) Determine necessary symmetry constraints for absolute instability, based on the antiperiodicity of the Stokes layer.

  (ii) Provide conclusive evidence for the existence of absolutely unstable behaviour in the Stokes layer.

  (iii) Determine the mechanisms responsible for establishing absolute instability and explain why pointwise growth is characterised by subharmonic behaviour.

  (iv) Formulate a relationship between the spatial periodicity 2Λ of the family-tree structure and the decomposition of the linear disturbance wavespectra.

1.4. *Paper structure*

The remainder of this paper is outlined as follows. The basic state and nondimensionalisation are discussed in §2, followed by the formulation for Floquet stability theory in §3. In §4, the Briggs method is introduced and discussed, with the derivation of an integral solution in §4.1, the development of pinch-points in §4.2, and symmetry arguments in §4.3. In §5, results are discussed for the Stokes layer, demonstrating agreement with

the symmetry constraints and providing insight into the key features described in §1.2. Finally, conclusions and suggestions for future work are presented in §6.

2. Base flow

Although we are primarily interested in the stability of linear disturbances in the semi-infinite Stokes layer, the subsequent modelling is carried out in a two-dimensional channel, as it was shown by Blennerhassett & Bassom (2006) that disturbance behaviour in a sufficiently wide channel is almost identical to that found in the semi-infinite configuration. Moreover, the finite domain is a more natural setting for the spectral numerical methods implemented herein.

Consider the two-dimensional flow of a viscous, incompressible fluid that is bounded between two infinite parallel plates, located a distance $2d$ apart. Each plate oscillates sinusoidally along the dimensional x^*-direction with a velocity

$$U_w = U_s \cos(\omega t), \qquad (2.1)$$

for a frequency of oscillation ω and velocity amplitude U_s. The motion of the bounding plates establishes a uni-directional flow that moves back and forth.

A non-dimensional basic state is obtained by defining the rescaled time $\tau = \omega t$, while units of velocity and length are scaled on U_s and the Stokes layer thickness $\delta = \sqrt{2\nu/\omega}$, respectively. Hence, if y denotes the direction normal to the bounding surfaces, the non-dimensional base flow is given as

$$\boldsymbol{U} = (U_B(y, \tau), 0), \qquad (2.2a)$$

where

$$U_B(y, \tau) = \mathrm{Re}\left[\frac{\cosh((1+i)y)}{\cosh((1+i)h)}\mathrm{e}^{i\tau}\right] = u_1\mathrm{e}^{i\tau} + \bar{u}_1\mathrm{e}^{-i\tau}. \qquad (2.2b)$$

Here $h = d/\delta$ is the non-dimensional channel half-width, with $h = 16$ for the subsequent investigation (the semi-infinite configuration is well approximated when $h > 14$, Blennerhassett & Bassom 2006; Thomas *et al.* 2015). Additionally, the Reynolds number of the flow is defined as

$$Re = \frac{U_s}{\sqrt{2\nu\omega}}, \qquad (2.3)$$

where ν denotes the kinematic viscosity of the fluid.

The basic state (2.2) is periodic in time with a period of 2π, i.e. $U_B(y, \tau + 2\pi) = U_B(y, \tau)$. Moreover, the flow is antiperiodic, meaning that a time-shift of half a period corresponds to an exact reversal of the flow, i.e. $U_B(y, \tau + \pi) = -U_B(y, \tau)$.

3. Floquet theory

As Squire's theorem has been extended to unsteady flows (Conrad & Criminale 1965; Von Kerczek & Davis 1974), the following analysis is restricted to the development of two-dimensional disturbances. Thus, the total velocity field is given as

$$(u, v) = (U_B, 0) + \epsilon\left(\frac{\partial\Psi}{\partial y}, -\frac{\partial\Psi}{\partial x}\right), \qquad (3.1)$$

where $\epsilon \ll 1$ and Ψ denotes the stream function that is decomposed as a Floquet mode

$$\Psi(x, y, \tau) = \psi(y, \tau)\exp(\mu\tau + i\alpha x) + \text{complex conjugate.} \qquad (3.2)$$

Here $\psi(y, \tau)$ is a 2π-periodic function in time, while $\alpha \in \mathbb{R}$ and $\mu \in \mathbb{C}$ denote the wavenumber and Floquet exponent, respectively. The growth or decay of the disturbance is included in the real part of μ and, since ψ is 2π-periodic, the disturbance is rescaled by the Floquet multiplier $\exp(2\pi\mu)$ after each full period of wall motion.

On substituting (3.1) into the Navier–Stokes equations and linearising in ϵ, the following governing equation for ψ is derived

$$\frac{\partial}{\partial \tau} \mathcal{L}\psi = \left[\frac{1}{2}\mathcal{L} - \mu - i\alpha ReU_B \right] \mathcal{L}\psi + i\alpha ReU_B'' \psi, \tag{3.3a}$$

with boundary conditions

$$\psi = \psi' = 0 \quad \text{on} \quad y = \pm h, \tag{3.3b}$$

where a prime denotes differentiation with respect to y and

$$\mathcal{L} = \frac{\partial^2}{\partial y^2} - \alpha^2. \tag{3.4}$$

Perturbations ψ are then decomposed into harmonics

$$\psi(y, \tau) = \sum_{n=-\infty}^{\infty} \psi_n(y) \exp(in\tau), \tag{3.5}$$

so that equating coefficients of harmonics in (3.3) results in an infinite system of equations

$$\left(\mathcal{L} - \alpha^2 - 2(\mu + in) \right) \mathcal{L}\psi_n = i\alpha Re \left(u_1 \left(\mathcal{L}\psi_{n-1} - 2i\psi_{n-1} \right) + \bar{u}_1 \left(\mathcal{L}\psi_{n+1} + 2i\psi_{n+1} \right) \right). \tag{3.6}$$

Given the normal mode form (3.2) and Fourier decomposition (3.5), the imaginary part of the Fourier exponent μ can be restricted to the interval $\mu \in [0, 0.5]$. Firstly, if μ is a solution, then so is $\mu + ik$ for $k \in \mathbb{Z}$. Secondly, due to the symmetry of the Stokes layer, Floquet modes occur as a complex conjugate pair $\mu = \mu_r \pm \mu_i$ that are matched to left- and right-travelling waves with equal growth. Moreover, disturbances are stationary in the instance the imaginary part of the Floquet exponent is zero, i.e. $\mu_i = 0$.

The system of equations (3.6) can be solved numerically using the pseudospectral techniques described by Trefethen (2000). Differential operators (that appear up to fourth order) are replaced by pseudospectral matrix approximations with each $\psi_n(y)$ replaced by a vector $\boldsymbol{\psi}_n$ of its function values on a Chebyshev mesh over the interval $-h \leqslant y \leqslant h$. Introducing matrix operators

$$\mathcal{L} \to \boldsymbol{L}, \quad \mathcal{L}^2/2 \to \boldsymbol{V} \quad \text{and} \quad \boldsymbol{P} = \boldsymbol{L}^{-1} u_1 (\boldsymbol{L} - 2i\boldsymbol{I}),$$

allows equation (3.6) to be rearranged as

$$-i\alpha Re\bar{\boldsymbol{P}}\boldsymbol{\psi}_{n+1} + (\boldsymbol{L}^{-1}\boldsymbol{V} - in\boldsymbol{I})\boldsymbol{\psi}_n - i\alpha Re\boldsymbol{P}\boldsymbol{\psi}_{n-1} = \mu\boldsymbol{\psi}_n, \tag{3.7}$$

where $\boldsymbol{I}$ is the identity matrix and $\bar{\boldsymbol{P}}$ is the complex conjugate of $\boldsymbol{P}$.

A finite system of equations is obtained by truncating the Fourier series (3.5), setting $\psi_n = 0$ for all $|n| > N$. The system of equations can then be written in a compact form by the concatenation of $\boldsymbol{\psi}_n$ into the vector

$$\phi^T = \left(\boldsymbol{\psi}_N^T, \boldsymbol{\psi}_{N-1}^T, \ldots, \boldsymbol{\psi}_0^T, \ldots, \boldsymbol{\psi}_{-N}^T \right). \tag{3.8}$$

In this manner, the problem is reduced to the eigenvalue problem

$$\boldsymbol{A}\phi = \mu\phi, \tag{3.9}$$

where $\boldsymbol{A}$ is a block-tridiagonal matrix (with block-size defined via the Chebyshev discretisation).

The number of harmonics N was carefully chosen to ensure that results were unchanged by further increases in N. In many cases $N = 300$ harmonics were necessary, while sufficient resolution along the wall-normal y-direction was achieved by using 100 Chebyshev points, resulting in a prohibitively large system (3.9). However, the least stable disturbances are expected to be symmetric about the channel centre (as per Blennerhassett & Bassom 2006). Thus, the size of the system can be significantly reduced by considering only even Chebyshev functions. Finally, since the block-tridiagonal matrix contains mostly zeros, the eigenvalue problem is efficiently solved using the sparse matrix eigenvalue routine in MATLAB. Further details of the derivation and numerical procedure are given in Blennerhassett & Bassom (2006) and Ramage (2017).

4. The Briggs method

The Floquet approach, described above, allows us to determine the asymptotic temporal characteristics of disturbances with a fixed streamwise wavenumber α, when the basic state is temporally periodic. On the other hand, the leading order behaviour of the integral solution, defined below, allows us to classify unstable disturbances as either convectively unstable (those that decay at each point in space) or absolutely unstable (those that grow at every spatial location).

In this section, the derivation of the integral solution that describes disturbances in two-dimensional flows is presented. Subsequently, the method in which the leading order behaviour is determined, by locating pinch-points in the complex α-plane, is described. The approach is based upon the method outlined in Brevdo & Bridges (1997) for temporally periodic media and is reproduced here to demonstrate the applicability to the time-periodic Stokes layer.

The Navier–Stokes equations are utilised to establish a single governing equation for the evolution of disturbances in the Stokes layer (2.2). The disturbance equation is again formulated in terms of a streamfunction ψ, similar to (3.3), except the full streamwise x and time τ dependence are now retained. The wall-normal y-direction then undergoes a discretisation, such as the Chebyshev method outlined in §3. Hence, the y-dependent streamfunction ψ is replaced with a vector $\boldsymbol{\psi}$ dependent only on x and τ, while operators denoting differentiation with respect to y are replaced with matrix approximations. The discrete approximation to the jth y-derivative will be denoted here by $\boldsymbol{D}^j$. The resulting disturbance equation is given as

$$\left[\frac{\partial}{\partial \tau} \left(\frac{\partial^2}{\partial x^2} \boldsymbol{I} + \boldsymbol{D}^2 \right) + Re\boldsymbol{U}(\tau) \frac{\partial^2}{\partial x^2} \left(\frac{\partial^2}{\partial x^2} \boldsymbol{I} + \boldsymbol{D}^2 \right) - Re\boldsymbol{U}''(\tau) \frac{\partial}{\partial x} \boldsymbol{I} - \right.$$

$$\left. \frac{1}{2} \left(\frac{\partial^2}{\partial x^2} \boldsymbol{I} + \boldsymbol{D}^2 \right)^2 \right] \boldsymbol{\psi}(x, \tau) = \boldsymbol{g}(x, \tau), \quad (4.1)$$

where $\boldsymbol{I}$ denotes the identity matrix and $\boldsymbol{g} = \boldsymbol{g}(x, \tau)$ describes an impulsive forcing. The basic state is included in the matrices $\boldsymbol{U}(\tau)$ and $\boldsymbol{U}''(\tau)$, which contain the discrete vector expressions of $U_B(y, \tau)$ and $U_B''(y, \tau)$ along the diagonal.

Equation (4.1) is dependent on the streamwise x-direction and time τ, with coefficients that are periodic in τ. The initial condition is defined as

$$\boldsymbol{\psi}(x, 0) = \boldsymbol{\psi}_0(x), \tag{4.2}$$

with

$$\boldsymbol{\psi}_0(x) \to 0 \quad \text{as} \quad x \to \pm\infty. \tag{4.3}$$

Furthermore, it is assumed that

$$\boldsymbol{\psi}(x,\tau) \to 0 \quad \text{as} \quad x \to \pm\infty \quad \text{for all } \tau. \tag{4.4}$$

4.1. *Integral solution*

The integral solution to (4.1) is derived following the procedure described by Brevdo & Bridges (1996) for spatially periodic flows and Brevdo & Bridges (1997) for temporally oscillating flows. A complete outline of the derivation is included in Ramage (2017), but for brevity, only the main points are described here, including the definitions for the Fourier and Laplace transforms, and the integral expression for $\boldsymbol{\psi}$.

First, a Fourier transform is applied to the streamwise x-direction

$$\boldsymbol{w}(\alpha) = \int_{-\infty}^{\infty} \boldsymbol{w}(x)\mathrm{e}^{-i\alpha x}\,\mathrm{d}x \quad \text{and} \quad \boldsymbol{w}(x) = \frac{1}{2\pi}\int_{-\infty}^{\infty}\boldsymbol{w}(\alpha)\mathrm{e}^{i\alpha x}\,\mathrm{d}\alpha, \tag{4.5a,b}$$

where α again denotes the streamwise wavenumber that is now allowed to be complex.

Following the application of Floquet theory, a Laplace transform is utilised, which is where the current approach differs from that presented in Brevdo & Bridges (1996, 1997). The frequency ω used in Brevdo & Bridges (1997) is replaced here by the Floquet exponent μ. One reason for the change in notation is for consistency with the Floquet method presented in §3. A second reason is that for Floquet modes (3.2), the term 'frequency' is imprecise since each Floquet mode contains a range of harmonic frequencies. The notation used here can be reconciled with that of Brevdo & Bridges (1997) by setting $\omega = -i\mu$, so that the subsequent analysis in the complex μ-plane is a 90° rotation of the complex ω-plane.

The Laplace transform used here has the form

$$\boldsymbol{w}(\mu) = \int_0^{\infty}\boldsymbol{w}(\tau)\mathrm{e}^{-\mu\tau}\,\mathrm{d}\tau \quad \text{and} \quad \boldsymbol{w}(\tau) = \frac{1}{2\pi}\int_{\sigma-i\infty}^{\sigma+i\infty}\boldsymbol{w}(\mu)\mathrm{e}^{\mu\tau}\,\mathrm{d}\mu, \tag{4.6a,b}$$

where σ in the integral limits of (4.6b) is selected so that the inversion contour lies to the right of all poles of the integrand in the complex μ-plane. (In the subsequent discussion it will be demonstrated that this ensures causality is satisfied.)

Following the application of the inverse Fourier and Laplace transforms, the integral solution for $\boldsymbol{\psi}$ is given as

$$\boldsymbol{\psi}(x,\tau) = \frac{1}{4\pi^2}\int_F \boldsymbol{Q}(\alpha,\tau)\int_L \frac{\boldsymbol{G}(\alpha,\mu)}{D(\alpha,\mu)}\exp(\mu\tau + i\alpha x)\,\mathrm{d}\mu\,\mathrm{d}\alpha, \tag{4.7}$$

where the inversion contours for the Fourier and Laplace transforms are denoted by $F = (-\infty, \infty)$ and $L = (\sigma - i\infty, \sigma + i\infty)$, respectively. The periodicity of the problem manifests in the function $\boldsymbol{Q}$, which is periodic in time τ with the same period as the basic state (2.2). Moreover, $\boldsymbol{Q}$ and $\boldsymbol{G}$ are non-singular (Brevdo & Bridges 1996, 1997). Thus, the integrand of (4.7) only has poles when the *dispersion relation* $D(\alpha,\mu) = 0$. When this condition is satisfied, the Floquet exponent μ represents an eigenvalue of (3.3) for a given wavenumber α. Therefore, the solution to the stability equation (3.3) is equivalent to finding the set of complex-valued μ that satisfy the dispersion relation $D(\alpha,\mu) = 0$ for fixed α.

The integral solution (4.7) can be used to describe two particular features of linear disturbances in the Stokes layer:

(i) The temporal evolution of the disturbance maximum.

(ii) The behaviour about fixed streamwise x-locations.

Thus, it is possible to classify the impulse response as stable, convectively unstable or absolutely unstable.

4.2. *Pinch-points*

Consider a solution to the disturbance equation (4.1) for an impulsive forcing g that is localised in both the spatial x-direction and in time τ, with g set to zero for $\tau < 0$. The corresponding solution is referred to as the *impulse response*, and is classified as stable if it decays in the asymptotic limit, whereby the total flow returns to the unperturbed basic state (2.2). On the other hand, if the solution grows it is unstable. An unstable solution can be further classified as convective or absolute, depending on the behaviour about fixed spatial x-locations. Unstable disturbances that decay at each x-position and convect away from the region of interest are convectively unstable, whereas a disturbance that grows about every x-location is absolutely unstable. While it might be concluded that the overall growth or decay of the solution to (4.1) is matched to the least-stable Floquet mode (3.2), the classification of the impulse response as being convective or absolute requires further consideration using the Briggs (1964) method.

The application of the Briggs method to the stability of steady shear flows is well documented (Gaster 1968; Lingwood 1997; Schmid & Henningson 2001; Huerre 2002) and for temporally periodic flows the process remains broadly unchanged, provided the time-dependence of the term Q in (4.7) is treated appropriately. However, a significant result of the subsequent investigation is the manner in which the existence of absolute instability is constrained by antiperiodicity. Moreover, the symmetry arguments used here to demonstrate this behaviour rely on an in-depth understanding of Briggs' method. Thus, an overview of the procedure outlined by Brevdo & Bridges (1997), that differs from the Briggs (1964) method through the inclusion of the time-periodic term Q, is presented below in order to contextualise the subsequent analysis.

The approach for characterising unstable disturbances is equivalent to that presented by Brevdo & Bridges (1997) with the exception of the rotation in the complex frequency plane that arises as a consequence of the differing representations of the temporal component of the perturbation. Equation (4.7) is evaluated for contours F and L in the respective complex α- and μ-planes, which are indicated by the respective horizontal and vertical red lines in figure 2. Closure of the two contours, F and L, is then achieved by adding a contour that connects the respective end-points. Since the integrand is zero along this closure, the integral solution (4.7) along the straight-line open contour is equivalent to that obtained over the closed contour. Thus, by Cauchy's residue theorem, the integral is the sum of the residues of the poles contained within the closed contour.

In the complex α-plane, depicted in figure 2(a), the integrand in (4.7) decays as $\alpha_i \to \infty$ for $x > 0$. Thus, the horizontal F contour can be closed by a semi-circular contour of infinite radius in the upper half-plane. Hence, when $x > 0$, the integral along F is determined by summing the residues of poles in the upper half-plane. Similarly, if $x < 0$, closure is achieved by a semi-circular contour in the lower half-plane and the integral along F is given by summing the residues of poles in the lower half-plane.

For each $\alpha \in F$ there are μ-roots to the dispersion relation $D(\alpha, \mu) = 0$ that correspond to poles of the integrand in (4.7). Taking the loci of these poles for all $\alpha \in F$ establishes $\mu(F)$ curves in the complex μ-plane. The $\mu(F)$ curve located furthest to the right in the complex μ-plane is illustrated by the solid purple curve in figure 2(b). The vertical L
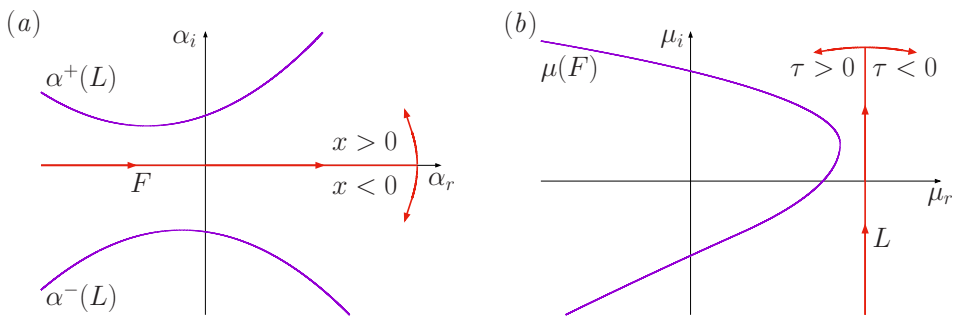
FIGURE 2. Sketches illustrating the initial set-up for Briggs' method. (a) Complex α-plane. (b) Complex μ-plane.

contour is then chosen to lie to the right of this curve by selecting the real part as

$$\sigma > \max\left\{\mu_r \mid D(\alpha, \mu) = 0, \ \forall \ \alpha \in \mathbb{R}\right\}. \tag{4.8}$$

Similar to the approach implemented for the F contour, closure of the L contour in the complex μ-plane is achieved via the addition of semi-circular contours to the left or right. The integrand in (4.7) decays as $\mu_r \to \infty$ for time $\tau < 0$. Thus, provided there are no poles to the right of the L contour, the integral must be zero. Hence, the disturbance is zero for all points in time prior to the application of the impulsive forcing $\boldsymbol{g}$. Therefore, it is necessary that σ is given by (4.8) to satisfy causality. For time $\tau > 0$, closure is achieved by a semi-circular contour to the left of the L contour. This closed contour then contains all poles of the integrand in (4.7).

For Floquet exponents $\mu \in L$, $\alpha^\pm(L)$ curves in the complex α-plane satisfy the dispersion relation $D(\alpha, \mu) = 0$ and describe poles of the integrand in (4.7), as depicted by the solid purple curves in figure 2(a). Initially, all poles are associated with spatial decay, while $\alpha^\pm(L)$ represent those curves that exhibit the slowest decay along the positive and negative valued x-directions.

The Fourier integral (4.5) in equation (4.7) is computed first, which is given as

$$\boldsymbol{\psi}(x^\pm, \mu) = \frac{1}{2\pi} \oint_{C_F^\pm} \boldsymbol{Q}(\alpha, \tau) \frac{\boldsymbol{G}(\alpha, \mu)}{D(\alpha, \mu)} \exp(i\alpha x^\pm) \, \mathrm{d}\alpha, \tag{4.9}$$

for some μ, where x^+ and x^- are shorthand for $x > 0$ and $x < 0$, respectively. Similarly, $C_F^\pm$ denotes the closed contour for a particular x value. Due to the adoption of this compact notation, two expressions are represented by (4.9). A single expression for all x is given by

$$\boldsymbol{\psi}(x, \mu) = H(x)\boldsymbol{\psi}(x^+, \mu) + H(-x)\boldsymbol{\psi}(x^-, \mu), \tag{4.10}$$

where $H(x)$ is the Heavyside function. Furthermore, by Cauchy's residue theorem

$$\boldsymbol{\psi}(x^\pm, \mu) = \pm i \sum_{k=1}^{\infty} \boldsymbol{Q}\left(\alpha_k^\pm(\mu), \tau\right) \frac{\boldsymbol{G}\left(\alpha_k^\pm(\mu), \mu\right)}{\frac{\partial D}{\partial \alpha}\left(\alpha_k^\pm(\mu), \mu\right)} \exp(i\alpha_k^\pm(\mu) x^\pm), \tag{4.11}$$

where $\alpha_k^+(\mu)$ and $\alpha_k^-(\mu)$ are the roots of the dispersion relation $D(\alpha, \mu) = 0$ in the upper and lower halves of the complex α-plane, respectively.

On solving the Fourier integral (4.9), the Laplace integration (4.6) is carried out. This is achieved by deforming the L contour to the left in the complex μ-plane. To illustrate this behaviour, we consider one particular μ value on L with a fixed imaginary part μ_i.
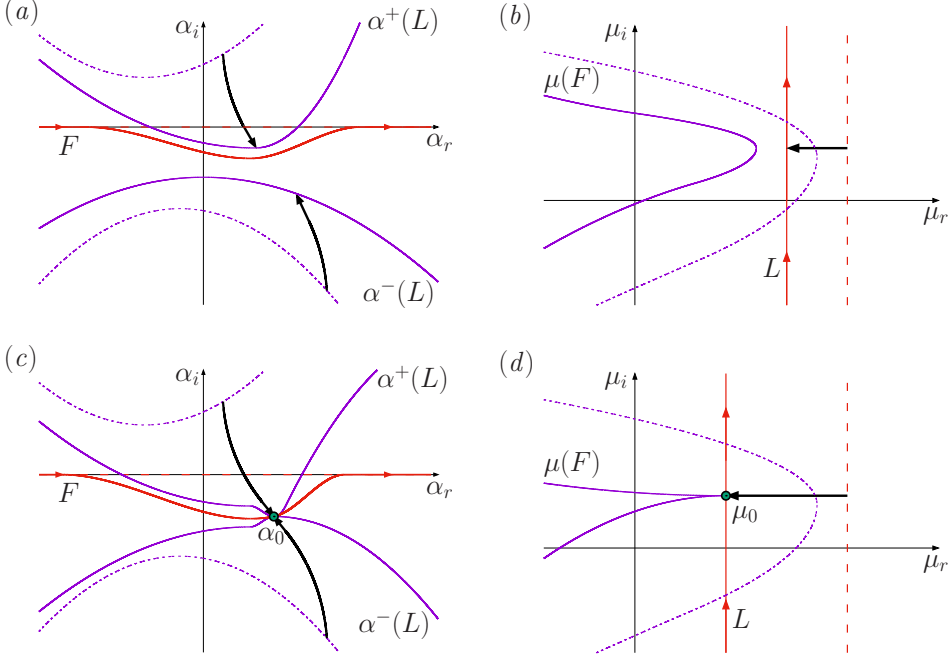
FIGURE 3. Sketches illustrating the pinching of the F contour in the complex α-plane as the contour L is shifted horizontally to the left in the complex μ-plane. Arrows indicate the behaviour brought about by the horizontal movement of a fixed Floquet exponent μ, dashed lines indicate the original contours and pole loci (as per figure 2), while solid curves demonstrate the deformations due to the leftward movement of the L contour. (a, b) μ is reduced until one α-root crosses the real α-axis. (c, d) $\mu = \mu_0$ corresponds to a collision of poles at α_0.

The corresponding real part, μ_r, is then reduced. The problem then simplifies to tracing the behaviour of poles in the complex α-plane as the real part of μ is shifted horizontally to the left. Figure 3 demonstrates both the behaviour about a fixed μ_i value and the overall deformation of the contours and curves when all μ_i are considered. The leftwards shift of a fixed μ value and the corresponding movement of the α-roots are illustrated by arrows in the respective μ- and α-planes; figure 3(a, b). The deformation of the L contour in the μ-plane and that of the corresponding F contour in the α-plane are made more obvious by the inclusion of the initial set-up (represented by dashed purple and red lines).

As the real part of the Floquet exponent is reduced, the resulting path will eventually cross the $\mu(F)$ curve, which describes the μ-roots of the dispersion relation $D(\alpha, \mu) = 0$ for $\alpha \in \mathbb{R}$; dashed purple curve in figure 3(b). Thus, at least one α-root of D lies along the real α-axis. Moving μ beyond the $\mu(F)$ curve allows one α-root to cross over the F contour and pass from one half of the complex α-plane to the other; as demonstrated by the arrow originating in the upper right quadrant in figure 3(a). Since a pole has shifted from one half of the complex α-plane to the other, there is a discontinuity in (4.11) for $\boldsymbol{\psi}$, with the jump being the size of the residue of this particular pole. However, an analytic continuation of $\boldsymbol{\psi}$ is achieved by deforming the F contour, as shown in figure 3(a), to ensure that all α-roots remain on their respective sides of F. The modification of the F contour results in a corresponding deformation of the $\mu(F)$ curve in figure 3(b).

By allowing for the deformation of the F contour, the horizontal shifting of the Floquet

exponent μ can be extended to smaller valued μ_r. However, in general, this procedure cannot be continued indefinitely. Once an α-root has crossed into the opposite half-plane, the leftwards shift to some $\mu = \mu_0$ is accompanied by the coalescence at α_0 of two poles originating in different halves of the complex α-plane, as demonstrated in figure 3(c, d). The F contour becomes pinched and passes through the pole at α_0, but cannot be deformed further without introducing discontinuities in ψ. Thus, a further reduction in μ_r is not possible. Note that a coalescence of α-roots originating within the same half-plane does not pinch the F contour.

The coalescence of two simple poles at α_0 results in a second order pole. Therefore, in addition to satisfying the dispersion relation

$$D(\alpha_0, \mu_0) = 0, \tag{4.12a}$$

it must also hold that

$$\frac{\partial D}{\partial \alpha}(\alpha_0, \mu_0) = 0. \tag{4.12b}$$

Thus, such collisions manifest as saddle points of the dispersion relation in the complex α-plane. Moreover, by inverting this relationship it becomes evident that the formation of a saddle point at α_0 is accompanied by the formation of a *cusp* at μ_0 (Kupfer *et al.* 1987), as illustrated by the solid purple curve in figure 3(d).

In equation (3.3), which is equivalent to the dispersion relation $D(\alpha, \mu) = 0$, the wavenumber α appears to the fourth order, while the Floquet exponent μ is linear. Since the matrices in the eigenvalue problem (3.9) are very large, it was computationally impossible to determine α for a given μ using the currently available computational resources. Hence, it was not feasible to locate saddle points of the dispersion relation in the complex α-plane. Nevertheless, utilising existing methods for computing μ for a given α, the corresponding cusps of the dispersion relation in the complex μ-plane may be located.

Using a Taylor series expansion for ψ about α_0, it may be shown that if α_0 is formed by the collision of two poles originating in the opposite halves of the α-plane, then it contributes to the expressions (4.9)–(4.11) for both positive and negative valued x. Hence, the parameter set (α_0, μ_0) contributes to the pointwise asymptotic behaviour of the disturbance. A similar argument can be used to demonstrate that if α_0 represents the collision of two poles originating in the same half-plane, there is a cancellation effect and the collision does not contribute to the asymptotic behaviour (Huerre 2002). The condition that the collision occurs between poles originating in opposite half-planes is known as the *collision criteria* (Brevdo & Bridges 1997).

Finally, the Laplace integration in (4.7) is carried out along a contour that lies to the right of every μ_0; there can be multiple such branch points, potentially a continuum, due to the continuous choice of μ_i at the start of the procedure. For a collision that satisfies the collision criteria, the leading order behaviour is then described by

$$\psi(x, \tau) \sim \frac{-i\boldsymbol{Q}(\alpha_0, \tau)\boldsymbol{G}(\alpha_0, \mu_0)}{\sqrt{2\pi\tau \dfrac{\partial D}{\partial \mu}(\alpha_0, \mu_0) \dfrac{\partial^2 D}{\partial \alpha^2}(\alpha_0, \mu_0)}} \exp\left(i\alpha_0 x + \mu_0 \tau\right), \tag{4.13}$$

where α_0 is the location of the pinch-type saddle point in the complex α-plane and μ_0 is the corresponding cusp location. While there are notionally multiple such values, the leading order behaviour of (4.13) is described by the pair (α_0, μ_0) for which μ_0 has the greatest real part. It is possible to account for lower order behaviour by considering a superposition of similar expressions for further (α_0, μ_0) pairs.

The expression for the streamfunction ψ, as given in (4.13), matches the Floquet mode decomposition given in (3.2), up to a multiplication by a factor $1/\sqrt{\tau}$. Pointwise temporal growth occurs if $\mathrm{Re}\{\mu_0\} > 0$, while $\mathrm{Re}\{\mu_0\} < 0$ corresponds to pointwise decay. In the former instance, the disturbance is classified as absolutely unstable, while in the latter case the disturbance is either convectively unstable or stable (depending on the growth or decay of the disturbance maximum).

4.3. *Symmetry constraints*

In addition to being periodic with a period 2π, the temporal variation of the basic state (2.2) is antiperiodic with an antiperiod π; i.e. $U_B(y, \tau + \pi) = -U_B(y, \tau)$. Thus, the distinction between the upstream and downstream x-directions is blurred, and the location of the roots of the dispersion relation $D(\alpha_0, \mu_0) = 0$ are constrained. This behaviour is illustrated by considering the governing perturbation equation (3.3), that is equivalent to the dispersion relation, whereby the solution is characterised by the complex-valued wavenumber α, Floquet exponent μ, and eigenfunction ψ:

$$(\alpha, \mu, \psi(y, \tau)). \tag{4.14a}$$

On taking the complex conjugate of (3.3), the governing perturbation equation remains unchanged but the solution is now characterised as

$$\left(-\bar{\alpha}, \bar{\mu}, \bar{\psi}(y, \tau)\right), \tag{4.14b}$$

where $\bar{z}$ denotes the complex conjugate of z. The existence of the solution (4.14a) implies the existence of the solution (4.14b), and this relationship holds irrespective of the antiperiodicity of the flow. Returning to (3.3) and applying a time-shift of half a period, $\tau \to \tau + \pi$, the sign of the basic state is reversed and the asymptotic behaviour for large time τ is unchanged. Thus, the solution is given as

$$(-\alpha, \mu, \psi(y, \tau + \pi)). \tag{4.14c}$$

The existence of the solution (4.14a) implies the existence of the solution (4.14c) when antiperiodicity holds. Applying both complex conjugation and a time shift of half a period to (3.3), the solution is characterised as

$$\left(\bar{\alpha}, \bar{\mu}, \bar{\psi}(y, \tau + \pi)\right). \tag{4.14d}$$

It follows from the related solutions (4.14) that for any given pair (α, μ) that satisfy (3.3),

$$D(\alpha, \mu) = 0 \implies \begin{cases} D(\bar{\alpha}, \bar{\mu}) &= 0, \\ D(-\alpha, \mu) &= 0, \\ D(-\bar{\alpha}, \bar{\mu}) &= 0, \end{cases} \tag{4.15}$$

for any antiperiodic flow.

In the instance $\alpha \in \mathbb{R}$, such that $\bar{\alpha} = \alpha$, the set of relationships (4.15) reduce to

$$D(\alpha, \mu) = 0 \implies \begin{cases} D(\alpha, \bar{\mu}) &= 0, \\ D(-\alpha, \mu) &= 0, \\ D(-\alpha, \bar{\mu}) &= 0. \end{cases} \tag{4.16}$$

Hence, for any $\alpha \in \mathbb{R}$, the μ-roots of the dispersion relation $D(\alpha_0, \mu_0) = 0$, appear in complex conjugate pairs. In terms of Briggs' method, this implies that the $\mu(F)$ curve, plotted in figure 2(b), is symmetric about the real μ-axis.

A similar argument can be established for Floquet exponents μ, once the harmonic

decomposition of μ in (3.5) has been taken into account. The imaginary part of the Floquet exponent, μ_i, is only given modulo one, since an integer shift is equivalent to a relabelling of the harmonics. Thus,

$$D(\alpha, \mu) = 0 \implies D(\alpha, \mu + ik) = 0, \tag{4.17}$$

for all integers k. Moreover, in the instance that μ_i is a multiple of $1/2$, complex conjugation is equivalent to an integer shift in μ_i. Therefore,

$$D(\alpha, \mu) = 0 \implies D(\alpha, \bar{\mu}) = 0, \tag{4.18}$$

where, restricting our interest to the interval $\mu_i \in [0, 1)$ gives

$$\mu = \mu_r + i \left\{ 0, \frac{1}{2} \right\} \quad \text{for} \quad \mu_r \in \mathbb{R}. \tag{4.19}$$

On applying the above symmetries, it follows that for all μ of the form (4.19), the set of relationships (4.15) reduces to

$$D(\alpha, \mu) = 0 \implies \begin{cases} D(\bar{\alpha}, \mu) &=& 0, \\ D(-\alpha, \mu) &=& 0, \\ D(-\bar{\alpha}, \mu) &=& 0. \end{cases} \tag{4.20}$$

In the pinch-point analysis described above, the imaginary part of μ is fixed and the α-roots of the dispersion relation $D(\alpha, \mu) = 0$ are traced as the real part of μ is shifted horizontally to the left (recall §4.2). When the imaginary part of μ is fixed such that $\mu_i = \{0, 1/2\}$, the movement of the α-roots is constrained by the symmetries of the base flow (2.2) and hence (4.20) holds. In particular, if the wavenumber α is a root of the dispersion relation $D(\alpha, \mu) = 0$, then so are the wavenumbers $\bar{\alpha}$, $-\alpha$ and $-\bar{\alpha}$. Thus, once μ comes into contact with the $\mu(F)$ curve and an α-root touches the real axis, the corresponding $\bar{\alpha}$-root must also touch the real axis. Similarly for $-\alpha$ and $-\bar{\alpha}$. Hence, the F contour is pinched along the real α-axis and no contour deformation is necessary. This behaviour is demonstrated in figure 4 for $\mu_i = 1/2$. Since the F contour is not deformed, neither is the $\mu(F)$ curve, though the existence of the saddle point at $\alpha_0 \in \mathbb{R}$ (and $-\alpha_0$) indicates a cusp at μ_0, as illustrated in figure 4(b). Moreover, there is a cusp indicated for $\mu_i = 0$, by the same argument. Note that the $\alpha^{\pm}(L)$ curves are not symmetric, even though the movement of the α-roots associated with $\mu_i = \{0, 1/2\}$ are symmetric along both axes.

The existence of these pinch-points is assured by the process outlined in §4.2, when the $\mu(F)$ curve is well defined for $\mu_i = \{0, 1/2\}$. The L contour in figure 2(b) contains all possible values of μ_i, including 0 and $1/2$, while the $\mu(F)$ curve (corresponding to $\alpha \in \mathbb{R}$) must lie to the left of the L contour to satisfy causality. Furthermore, as μ is shifted to the left for $\mu_i = \{0, 1/2\}$, the $\mu(F)$ curve is eventually reached. Hence, by the symmetry arguments described above, a collision of complex conjugate α-roots occurs. There is a possibility that in some antiperiodic flows the $\mu(F)$ curve is not well defined for $\mu_i = \{0, 1/2\}$, i.e. there are no real α corresponding to these particular μ_i values. However, this was not the case for the Stokes layer studied herein and so is not discussed any further, but is highlighted as a potential factor in other antiperiodic flows.

The above analysis indicates that saddle points of the dispersion relation $D(\alpha, \mu) = 0$, satisfying the collision criteria, occur whenever $\alpha \in \mathbb{R}$ and $\mu_i = \{0, 1/2\}$; collisions emerge between complex conjugate α-roots. Moreover, for these particular μ_i values, the collision of two α-roots originating within the same half-plane onto the real axis will be accompanied by the collision of their respective complex conjugates in a four-way
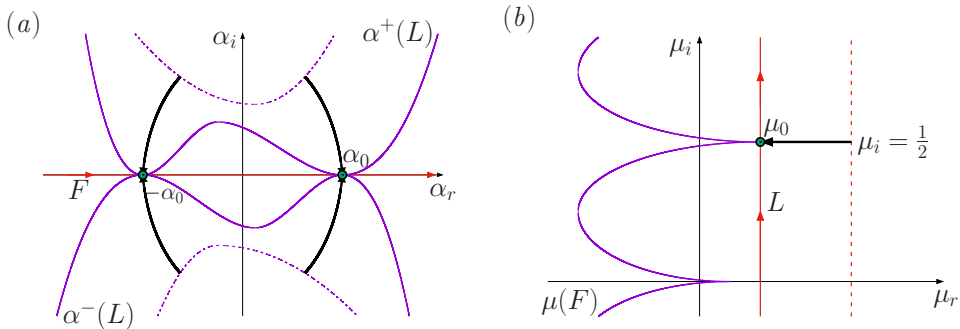
FIGURE 4. Sketches illustrating the pinching of the F contour along the real α-axis, when $\mu = \mu_r + i/2$. (*a*) Complex α-plane. (*b*) Complex μ-plane. For the horizontal line extending from the L contour to the $\mu(F)$ curve, there is a matching symmetric movement of the α-roots that form collisions along the real α-axis about $\pm\alpha_0$.

collision. Thus, all saddle points of the dispersion relation with these characteristics must satisfy the collision criteria.

Further collisions may occur for $\mu_i \neq \{0, 0.5\}$ (as μ crosses the $\mu(F)$ curve) that bring about greater pointwise growth than that found for $\mu_i = \{0, 1/2\}$. In such instances, this may necessitate a deformation of the F contour and establish a pinch-point with the $\text{Re}\{\mu_0\}$ greater than that found using the symmetry arguments. However, while such behaviour may be significant for other flows, this was not found for the Stokes layer: the rightmost point of the $\mu(F)$ curve was matched to a cusp with $\alpha \in \mathbb{R}$ and $\mu_i = 0$ in every case considered.

4.4. *Development of the disturbance maximum*

In addition to determining the disturbance development about fixed spatial locations (via the Briggs method), the integral solution (4.7) provides insight into the leading order behaviour of the disturbance maximum. The stability of a disturbance ψ to an impulse g can be determined by generalising the problem to consider the leading order behaviour along an arbitrary spatiotemporal ray

$$x/\tau = V,$$

where V is constant.

In this setting, the leading order pointwise behaviour (deduced by the Briggs method) corresponds to $V = 0$. On the other hand, the temporal growth associated with the disturbance maximum is matched to the spatiotemporal ray $V = V_{\text{max}}$. The growth-rate along this particular ray is of interest as Ramage *et al.* (2020) report that the temporal growth about fixed spatial locations matches that of the disturbance maximum.

Similar to the arguments used for steady flows, the Floquet mode (3.2) that contributes towards the growth (or decay) of the disturbance along the ray V_{max} corresponds to $\alpha \in \mathbb{R}$ and

$$\frac{\partial \mu_r}{\partial \alpha} = 0. \tag{4.21}$$

This particular result is derived by solving the integral equation (4.7) along a spatiotemporal ray by the method of steepest-descent (refer to Ramage 2017, for details). It follows that the asymptotic temporal growth of the disturbance maximum can be determined by plotting the real part of the Floquet exponent μ as a function of the real wavenumber α, and selecting the maximum.

For antiperiodic flows, such as (2.2), the asymptotic temporal growth of the disturbance maximum and the asymptotic pointwise growth correspond to $\alpha \in \mathbb{R}$. Hence, the growth-rate along the ray $V_{\max}$ and the pointwise growth-rate along $V = 0$ can be equivalent, provided the collision location along the real α-axis corresponds to a local maximum of μ_r.

5. Results

The impulse response of linear disturbances in the Stokes layer was first investigated by Thomas *et al.* (2014) and then subsequently by Ramage *et al.* (2020) via direct numerical simulations (DNS). It was revealed that the family-tree structure develops (as depicted in figure 1), which consists of a mother wavepacket giving birth to two daughter wavepackets during each period of wall motion. One wavepacket propagates to the left, while the second convects to the right. These two daughter wavepackets birth granddaughter wavepackets and so on, giving rise to the so-called family-tree formation. It was observed that the disturbance maximum propagates along successive wavepackets in the direction dictated by the phase of the wall motion at the time at which the impulsive forcing was applied (to the right in figure 1). Additionally, the spatial distance between adjacent wavepackets is fixed by the Reynolds number *Re*, and so granddaughter wavepackets manifest in the same streamwise x-location as the mother wavepacket, resulting in an increase in the disturbance magnitude every two periods of wall motion. Thus, subharmonic growth occurs about fixed spatial positions, i.e. pointwise growth with a periodicity twice that of the basic state. Furthermore, the temporal growth about fixed spatial locations was found to match the growth of the disturbance maximum. Hence, DNS results suggest that the Stokes layer is subject to an absolute form of instability. However, such behaviour can only be confirmed theoretically via the application of the Briggs criteria.

Harmonic and subharmonic behaviour can be associated with the imaginary part of the Floquet exponent μ in (4.19) that was highlighted as being significant in the symmetry arguments described above; recall $\mu_i = \{0, 1/2\}$. In the instance $\mu_i = 0$, a stationary Floquet mode of the form (3.2) has the same periodicity as the basic state (2.2), with behaviour described as *harmonic*. On the other hand, when $\mu_i = 1/2$, the imaginary part of the Floquet exponent can be absorbed into the periodic streamfunction ψ in (3.2), resulting in a period twice that of the basic state. This behaviour is *subharmonic* and describes the pointwise behaviour observed in the earlier DNS computations. These two particular cases are distinct from the more general Floquet mode form, in which the disturbance amplification is accompanied by a phase shift.

5.1. *Floquet analysis*

5.1.1. *Eigenspectra*

Before we undertake an investigation of absolute instability in the Stokes layer, a linear stability analysis is performed to validate the numerical scheme and to report on the complex stability characteristics first presented by Blennerhassett & Bassom (2002, 2006). Figure 5 displays a subset of the eigenvalues of (3.9) in the complex μ-plane, for the Reynolds number $Re = 750$ and wavenumbers $\alpha = 0.25, 0.35$ and 0.3747. Open red circular markers represent centre modes that were first reported in Von Kerczek & Davis (1974) and subsequently by Blennerhassett & Bassom (2006) for oscillatory flow in a channel. Multiple decaying centre modes γ (with a negative real component and a zero imaginary component) are found along the real μ-axis and then at $\mu = \gamma + ik$ for all
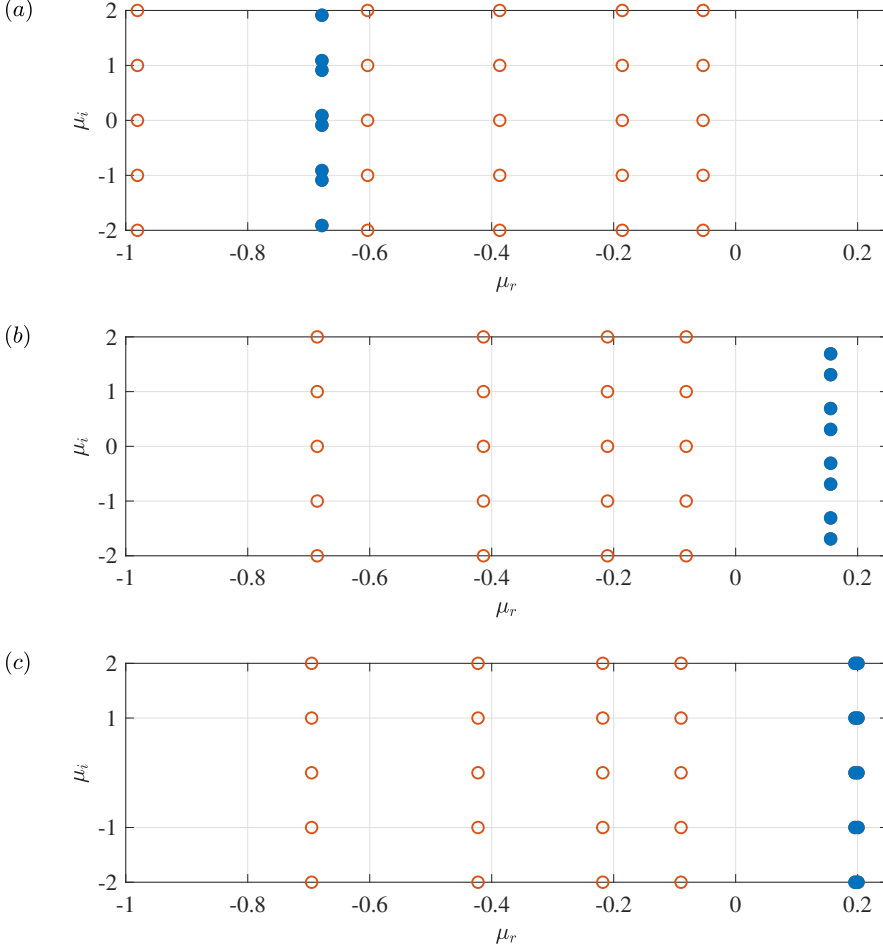
FIGURE 5. Floquet exponents μ in the complex μ-plane for the Reynolds number $Re = 750$ and wavenumbers (*a*) $\alpha = 0.25$, (*b*) $\alpha = 0.35$ and (*c*) $\alpha = 0.3747$. Solid blue circles are matched to the Stokes mode, while open red circles are matched to centre modes.

integers k. These particular perturbations are associated with disturbance development in the channel centre and are always linearly stable for the range of Reynolds numbers modelled in this study. Solid blue circular markers correspond to the Stokes mode that is of primary interest here. For each Floquet exponent μ there is a corresponding complex conjugate $\bar{\mu}$. This complex conjugate pair are then matched to left- and right-travelling waves with equal growth. Additionally, there are equivalent Floquet exponents $\mu + ik$ for all integers k. Hence, the imaginary part of the Floquet exponent can be restricted to the interval $\mu_i \in [0, 0.5]$ for the remainder of this study.

For the wavenumber $\alpha = 0.25$, the Floquet exponent μ has a negative real part, i.e. $\mu_r < 0$. Thus, the disturbance is linearly stable for this particular wavenumber. However, as α increases to 0.35 and 0.3747, the Floquet exponent crosses the $\mu_r = 0$ axis and
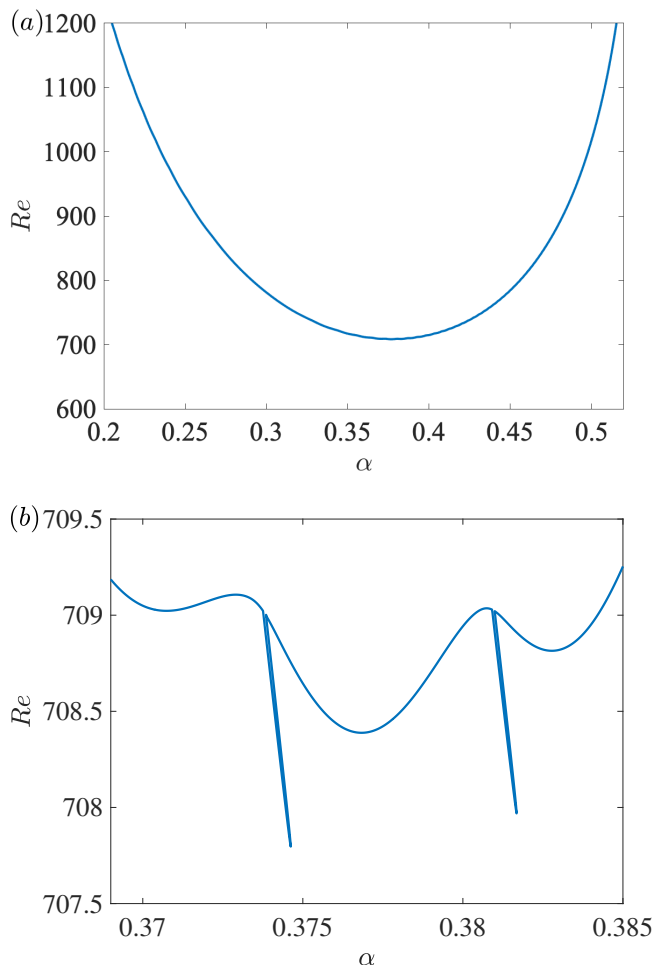
FIGURE 6. Neutral curve for linear instability in the (α, Re)-plane. (*a*) Large α-domain. (*b*) Reduced α-domain about the critical conditions for instability.

becomes positive, leading to linearly unstable behaviour. Interestingly, for $\alpha = 0.3747$, the left- and right-travelling waves (given by the complex conjugate pair μ and $\bar{\mu}$) coalesce to form two stationary waves but with marginally different growth rates. This particular phenomena was first discovered by Blennerhassett & Bassom (2002) and leads to the formation of *finger*-like structures along the neutral stability curve.

5.1.2. *Neutral stability curve*

Neutral points (α, Re) for linear instability were determined (i.e. $\mu_r = 0$), with sections of the neutral stability curve plotted in figure 6. In figure 6(*a*), the neutral curve is plotted over a large α-domain and appears smooth. Here (and for the remainder of this study) the analysis has been restricted to wavenumbers $\alpha \leqslant 0.52$, as following Blennerhassett & Bassom (2002), linearly unstable behaviour is not expected for larger valued α. The critical Reynolds number Re_c corresponds to the lowest point along this curve, below which all disturbances are linearly stable. In figure 6(*b*), the neutral curve is plotted over a reduced α-range, localised about the critical conditions for linear instability. The critical Reynolds number $Re_c = 707.84$ is located about the tip of one of the finger-like
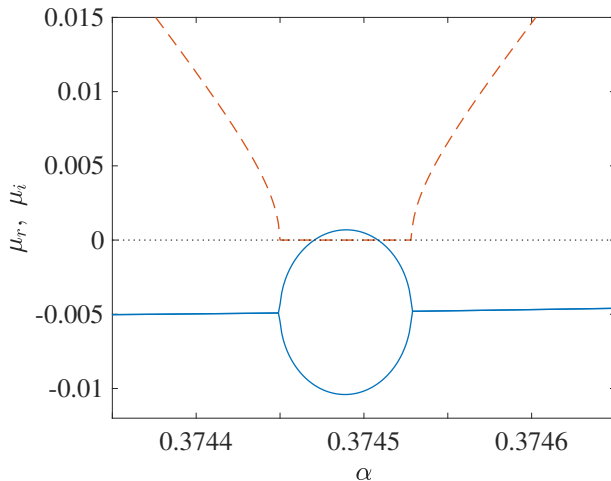
FIGURE 7. Variation of the real and imaginary parts of the Floquet exponent μ as a function of the wavenumber α in a region that $\mu_i = 0$. Here the Reynolds number $Re = 708$; solid and dashed lines depict the real μ_r and imaginary μ_i components.

protrusions that extend vertically downwards from the main body of the neutral stability curve. As reported in Blennerhassett & Bassom (2002), these finger-like features occur at regular wavenumber intervals and are matched to stationary disturbances, i.e. $\mu_i = 0$.

Figure 7 depicts the variation of the real (solid line) and imaginary (dashed line) parts of the Floquet mode μ as a function of the wavenumber α, for the Reynolds number $Re = 708$. Results are plotted about the region where linearly unstable stationary modes develop and corresponds to a horizontal cut through the leftmost finger in figure 6(b). There is a small wavenumber interval about $0.37445 < \alpha < 0.37455$ that μ_i is zero, leading to the emergence of stationary waves. Outside of this interval, μ_i is non-zero. (Note that for consistency with the presentation of figure 1 of Blennerhassett & Bassom 2002, when the Floquet exponent μ is complex, only eigenvalues corresponding to $\mu_i > 0$ are plotted in figure 7; the complex conjugate $\bar{\mu}$ has been omitted.) At the left end point of this interval, stable left- and right-travelling waves (corresponding to μ and $\bar{\mu}$) coalesce to form two stationary waves. Significantly, the two stationary waves have very different growth rates over this interval, with one becoming marginally unstable. This behaviour is consistent with the formation of the leftmost finger-like protrusion in figure 6(b). As the wavenumber α increases, the two stationary waves reestablish the two stable travelling waves with equal growth μ_r but opposite sign μ_i. This particular stability feature of the Stokes layer is not restricted to Floquet modes along the neutral stability curve, but is found throughout the (α, Re) parameter space.

5.1.3. *Temporal growth of the disturbance maximum*

Floquet calculations for the growth-rate μ_r are compared against the DNS computations of Ramage *et al.* (2020), who numerically determined the growth-rate of the disturbance maximum. Figure 8 depicts the variation of the Floquet growth-rate μ_r, for Reynolds numbers $Re = 700$ and $Re = 750$, over the wavenumber interval $\alpha \in [0, 0.5]$. The local maximum that satisfies condition (4.21) is indicated by a red cross marker. Within each subplot, magnified insets highlight those modes with the largest growth-rate μ_r. In both instances, the local maximum is located about the tip of a finger-like protrusion and are comparable with those structures found along the neutral stability curve in figure 6
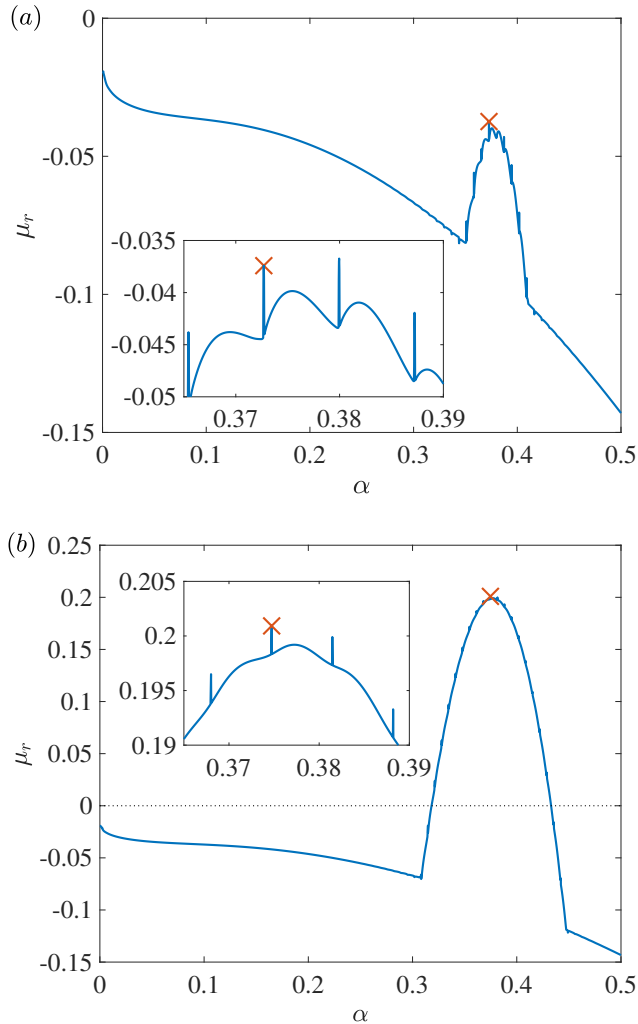
FIGURE 8. Floquet growth-rate μ_r as a function of the real wavenumber α for (*a*) $Re = 700$ and (*b*) $Re = 750$. The largest growth-rate that satisfies (4.21) is indicated by red cross markers. $(\alpha, \mu_r) = (0.3727, -0.0374)$ for $Re = 700$ and $(\alpha, \mu_r) = (0.3747, 0.2009)$ for $Re = 750$.

that are brought about by the appearance of stationary waves. In figure 8(*a*), larger (less negative) growth rates are observed for wavenumbers α near zero but correspond to the centre modes γ and have been disregarded as they do not satisfy the local maximum condition (4.21).

Table 1 compares those Floquet growth rates μ_r that achieve a maximum in figure 8 against the equivalent DNS computations obtained by Ramage *et al.* (2020). Growth rates agree to two decimal places, which is excellent given that the DNS calculations were based on measurements taken after a finite time interval. Thus, small differences are to be expected.

In both illustrations shown in figure 8, maximum growth rates are located at the tip of finger-like protrusions. Since these protruding features correspond to stationary waves with both $\mu_i = 0$ and $\alpha_i = 0$, which was highlighted in section 4.3 as implying the

Re	700	750
μ_r (Floquet)	-0.0374	0.2009
DNS	-0.0416	0.1982

TABLE 1. Floquet growth-rate μ_r for the least-stable mode with $\alpha \in \mathbb{R}$ (see figure 8), compared against the DNS computations of Ramage *et al.* (2020)

location of pinch-points in antiperiodic flows, this is an appropriate starting point for the search of absolutely unstable behaviour.

5.2. *Absolute instability*

5.2.1. *Approach I: $\alpha \in \mathbb{C}$*

As discussed in §4, those modes that contribute to the asymptotic pointwise growth of the impulse response and classify the disturbance as convectively or absolutely unstable can be determined by locating cusps of the dispersion relation $D(\alpha, \mu) = 0$ in the complex μ-plane. This is achieved by numerically solving the eigenvalue problem (3.3) and mapping solutions from the complex α-plane onto the complex μ-plane. Given the symmetry arguments outlined above for antiperiodic flows, cusps matched to $\alpha_i = 0$ and $\mu_i = \{0, 1/2\}$ satisfy the collision criteria and hence establish absolute instability.

The emergence of cusps in the complex μ-plane and absolutely unstable behaviour will be demonstrated first (and in the most detail) for the Reynolds number $Re = 750$, which corresponds to a strongly unstable disturbance, as illustrated by the positive Floquet growth-rate μ_r in figure 8(*b*) and table 1. Figure 9 depicts the two types of cusps that emerge, in which the imaginary part of the Floquet exponent μ is zero and a half, respectively. The two cusp formations were constructed by first locating regions within the stability parameter space that for $\alpha \in \mathbb{R}$ establish the least stable Floquet mode μ, with the imaginary part $\mu_i = 0$ or $\mu_i = 1/2$. The complex α-plane was then divided into a rectangular mesh grid about this point, as indicated by the horizontal and vertical black lines in figure 9(*a, c*). A very fine resolution was implemented, with step sizes $\Delta\alpha_r = 10^{-7}$ and $\Delta\alpha_i = 10^{-8}$ along the respective horizontal and vertical directions. As shown in figure 9(*b, d*), each grid point was then mapped via the solution to equation (3.9) onto the complex μ-plane. Those grid lines nearest to the cusps (in the complex μ-plane) are indicated by the red lines, with the cusp locations marked by the circular blue markers. The corresponding grid lines in the complex α-plane are given by the vertical red lines. In both instances, the cusp is matched to a real-valued wavenumber α (circular blue markers in figure 9(*a, c*)), while the real part of the Floquet exponent μ is positive, i.e. $\mu_r > 0$. Hence, by the symmetry arguments of §4.3, pointwise growth occurs, which demonstrates that the Stokes layer is absolutely unstable for $Re = 750$.

The cusp depicted in figure 9(*b*) corresponds to the tip of a finger-like protrusion in figure 8(*b*), where $\mu_i = 0$. For visual clarity this is re-plotted over a reduced wavenumber α-range in figure 10(*a*). This particular mode exhibits the greatest Floquet growth rate for the given Reynolds number: $\mu_r = 0.2009$ and $\alpha = 0.3747$. Hence, as $\mu_i = 0$ and $\mu_r > 0$, harmonic growth occurs for this particular parameter set. Further harmonic cusps, with $\alpha_i = \mu_i = 0$, were located about the tips of other finger-like protrusions, as demonstrated in figure 10(*a*) (red circular markers).

The illustration in figure 9(*d*) displays a cusp with $\mu_i \approx 1/2$ and is associated with subharmonic growth. Here $\mu_r = 0.1973$ and $\alpha = 0.3714$. Several additional subhar-
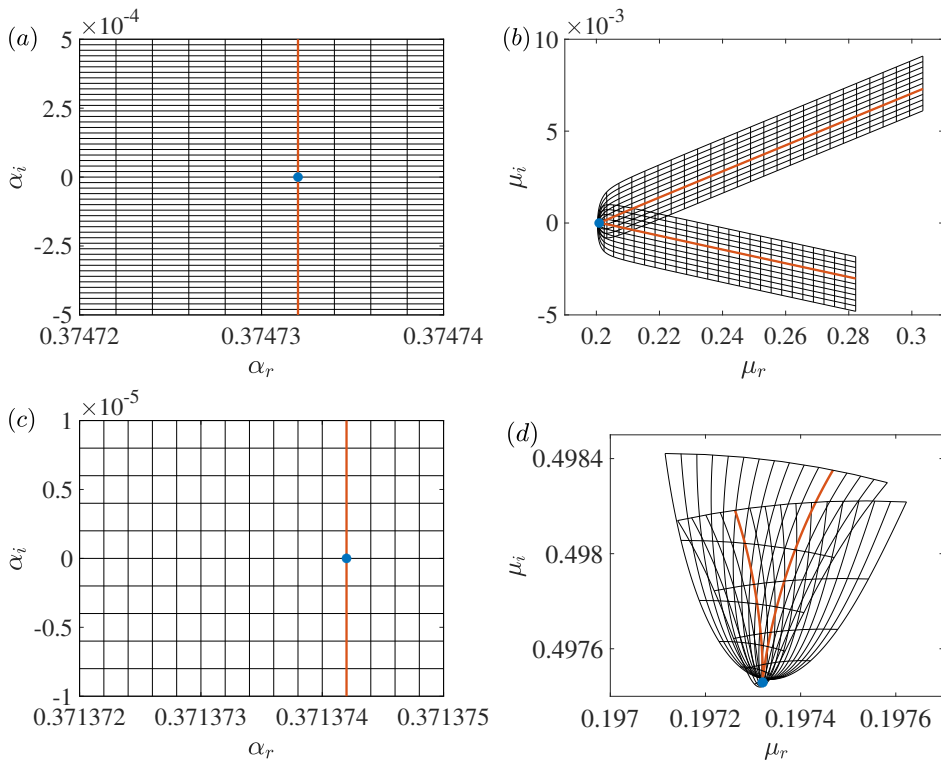
FIGURE 9. Rectangular mesh grids in the complex α-plane (a, c) are mapped via the dispersion relation $D(\alpha_0, \mu_0) = 0$ onto the complex μ-plane (b, d), revealing cusp formations. The cusp in (b) corresponds to $\mu_i = 0$ and the tip of a finger-like protrusion (as indicated in figure 10), while the cusp in (d) corresponds to $\mu_i = 1/2$ and is located about the mid-point between two adjacent fingers.

monic modes are indicated by yellow diamond markers along the curve in figure 10(a). Furthermore, these particular modes are located about the mid-point between adjacent finger-like protrusions. Hence, the pointwise growth of the disturbance, established for the Reynolds number $Re = 750$, is characterised by a set of both harmonic and subharmonic absolutely unstable modes. The location of all cusps found by the construction of the cusp-map diagrams, similar to figure 9, are reported in table 2. (Note that the cusp associated with the subharmonic mode, $\mu_i \approx 1/2$, is not found at exactly $\mu_i = 1/2$. Further discussion on this particular observation is included in §5.4.)

The four harmonic (red circles) and three subharmonic (yellow diamond) modes marked in figure 10(a) are the only absolutely unstable modes found using the cusp map method for the given range of wavenumbers α. Further cusps that establish absolute instability were located for smaller and larger valued α, at regular α-steps, but at smaller growth rates μ_r. All remaining modes depicted along the blue curve in figure 10(a) are matched to convectively unstable behaviour characterised by disturbances that propagate to the left or right only.

The distinction between convectively and absolutely unstable behaviour in the context of the time-periodic Stokes layer is made by comparing the development of the disturbance streamfunction ψ. In figure 11, contours of the real part of ψ are plotted in the $(\tau/2\pi, y)$-plane, for four successive wavenumbers $\alpha = 0.3731, 0.3747, 0.3764$ and 0.3781, with the imaginary part of the Floquet exponent $\mu_i = 0.25, 0, 0.25$ and 0.4975,

α_r	μ_r	μ_i
0.3680	0.1965	0.0000
0.3714	0.1973	0.4975
0.3747	0.2009	0.0000
0.3781	0.1991	0.4975
0.3815	0.1999	0.0000
0.3848	0.1953	0.4975

TABLE 2. Real part of the wavenumber α (with $\alpha_i = 0$) and Floquet exponents $\mu = \mu_r + i\mu_i$, associated with cusps for $Re = 750$. Cusps are indicated in figure 10 by circular and diamond markers.
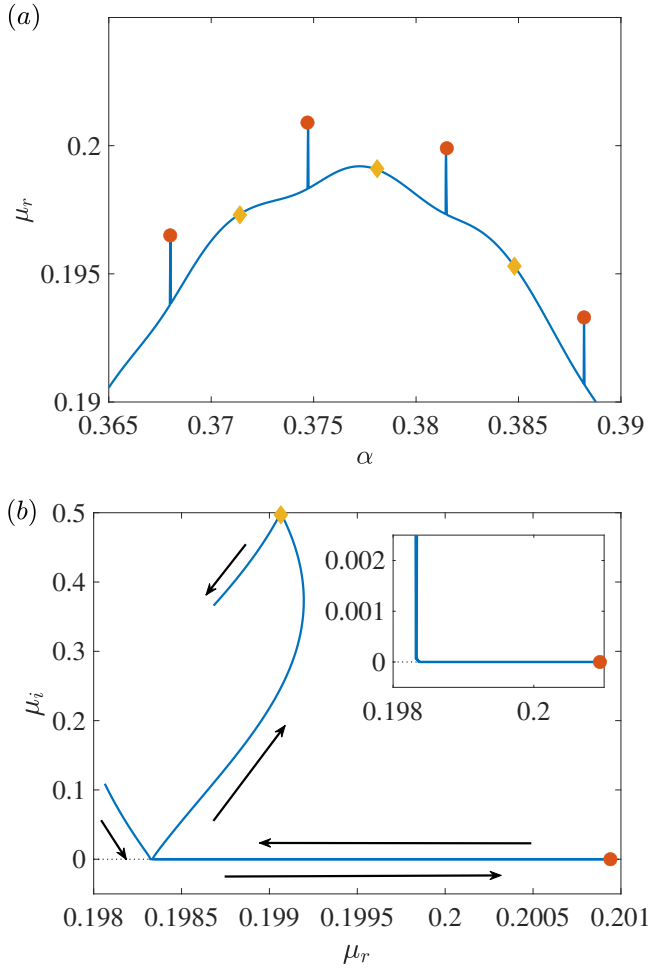

FIGURE 10. (*a*) Floquet growth-rate μ_r as a function of the wavenumber $\alpha \in \mathbb{R}$ for the Reynolds number $Re = 750$. Same as figure 8(*b*) but over a reduced α-range. (*b*) Path of the least-stable mode in the complex μ-plane, for $\alpha \in [0.374, 0.379]$. (Arrows indicate the direction of increasing α.) Red circular and yellow diamond markers indicate those locations matched to absolutely unstable harmonic and subharmonic modes, where $\mu_i = 0$ and $1/2$, respectively.
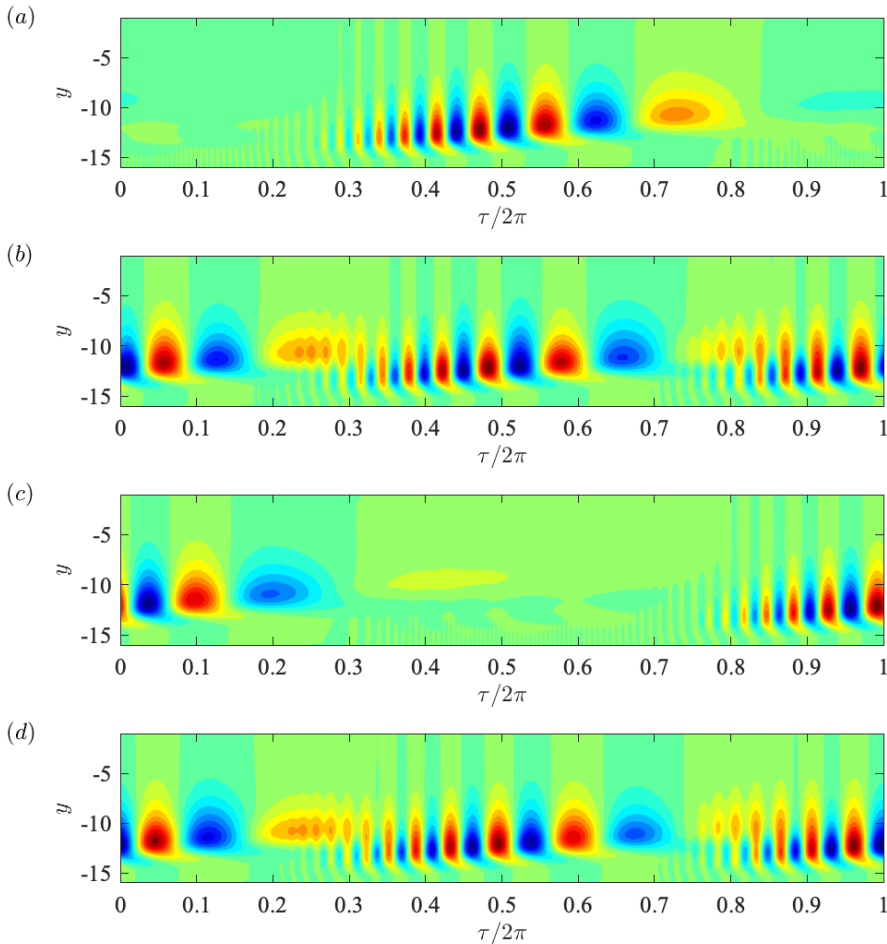
FIGURE 11. Contours of the real part of the disturbance streamfunction ψ over one period, for the Reynolds number $Re = 750$. (a) $\alpha = 0.3731$ and $\mu = 0.1976 + i0.2500$. (b) $\alpha = 0.3747$ and $\mu = 0.2009$. (c) $\alpha = 0.3764$ and $\mu = 0.1988 + i0.2500$. (d) $\alpha = 0.3781$ and $\mu = 0.1991 + i0.4975$. Each disturbance is normalised on its respective maximum complex-valued amplitude.

respectively. In each instance, the real part of the Floquet exponent is positive, leading to strong temporal growth. Additionally, each solution has been normalised on its respective maximum complex-valued amplitude $|\psi|$, while red and blue contours are matched to positive and negative valued ψ_r, respectively. Moreover, the corresponding solutions for the complex conjugate (with $\mu_i < 0$) bring about a time shift of π along the time axis.

All four plots share several common characteristics, consistent with the observations first made by Blennerhassett & Bassom (2002) and subsequently by Thomas (2020, 2021). For the four parameter settings considered, perturbations first appear within the boundary layer about either $\pi/4 \leqslant \tau_1 \leqslant \pi/2$ or $5\pi/4 \leqslant \tau_2 \leqslant 3\pi/2$. (The subscript 1 and 2 notation in τ has been introduced here to indicate the first or second time interval that

disturbances emerge during the periodic cycle.) Initially, each disturbance evolves with a high-frequency oscillation and grows along lines of constant $\tau - y$. A maximum amplitude is then realised near the boundary layer edge, about either the mid-point or end-point of the cycle that are matched to the wall velocity (2.1) achieving either a minimum or maximum. Further away from the wall, the disturbance diminishes and the frequency of oscillation decreases.

As noted by Blennerhassett & Bassom (2002), the upper bound on the time intervals τ_1 and τ_2 coincides with the velocity (2.1) of the bounding plate being zero. Moreover, it was shown by Thomas *et al.* (2014) that perturbations grow rapidly when the wall shear stress $U'_B(0, \tau)$ changes sign (see figure 1 of their paper). A negative to positive change in $U'_B(0, \tau)$ occurs at $\tau = \pi/4$ and coincides with a disturbance propagating to the right, while a left travelling disturbance appears at $\tau = 5\pi/4$ when $U'_B(0, \tau)$ reverses from a positive to a negative value. Hence, given these observations, disturbances for $\alpha = 0.3731$ and $\alpha = 0.3764$, plotted in figures 11(*a*) and 11(*c*), are found to propagate to the right and left, respectively. Thus, these particular travelling modes display convectively unstable characteristics, as they propagate in one direction only. (This is true for all modes with $0 < \mu_i \lessapprox 0.5$.) On the other hand, for the harmonic $(\alpha, \mu_i) = (0.3747, 0)$ and subharmonic $(\alpha, \mu_i) = (0.3781, 0.4975)$ modes plotted in figures 11(*b*) and 11(*d*), perturbations emerge about both time intervals τ_1 and τ_2, establishing disturbance development along both the left and right x-directions. Thus, the streamfunction ψ further demonstrates the significance of these particular modes in establishing absolutely unstable behaviour in the Stokes layer. Note that the behaviour of these two modes is still classified as harmonic and subharmonic when the full normal mode structure (3.2) has been accounted for, i.e. solutions in figure 11 are scaled by $\exp(\mu\tau)$.

The time interval that travelling modes $0 < \mu_i \lessapprox 0.5$ develop and the associated propagation direction is found to reverse as the wavenumber α increases. About the harmonic modes, the time interval changes from τ_1 to τ_2, leading to disturbances reversing direction and propagating from right to left. The opposite behaviour occurs near the subharmonic modes, with a τ_2 to τ_1 and left to right reversal taking place.

5.2.2. *Approach II: $\alpha \in \mathbb{R}$*

By constructing cusp-map diagrams, we have confirmed the existence of cusps in locations predicted by the symmetry arguments of §4.3, for the Reynolds number $Re = 750$. However, extending the cusp analysis to other Reynolds numbers is computationally demanding, as equation (3.9) must be solved many times in order to fully resolve curves in the complex μ-plane. (Recall that step sizes $\Delta\alpha_r = 10^{-7}$ and $\Delta\alpha_i = 10^{-8}$ were used to construct the mesh grid in figure 9(*a*, *c*).) Nevertheless, an alternative approach was implemented that allowed cusp locations to be determined more efficiently. Given the arguments presented in §4.3 and those solutions tabulated in table 2, we restrict the cusp analysis to $\alpha_i = 0$, with real wavenumber step sizes $\Delta\alpha_r = 2 \times 10^{-5}$; cusp locations are determined for $\alpha \in \mathbb{R}$ only. For instance, figure 10(*b*) depicts the path of Floquet modes in the complex μ-plane for wavenumbers $\alpha \in [0.374, 0.379]$, with arrows indicating the direction that α increases. The location of the most unstable harmonic and subharmonic cusps are then highlighted by circular and diamond markers, respectively. A smaller wavenumber step size $\Delta\alpha_r = 10^{-8}$ was implemented for the inset plot in figure 10(*b*), to fully resolve the behaviour near $\mu_i = 0$. This approach was used to locate the rightmost harmonic cusp in figure 10(*a*), which was not reported in table 2 using the cusp-map approach. The cusps found using this faster approach are given in table 3, with calculations in excellent agreement with those results presented in table 2.

The pointwise growth of the linear disturbance with $Re = 750$ is characterised by those

	α_r	μ_r	μ_i
$Re = 750$	0.3680	0.1962	0.0000
	0.3714	0.1973	0.4972
	0.3747	0.2006	0.0000
	0.3781	0.1991	0.4975
	0.3815	0.1999	0.0000
	0.3848	0.1953	0.4974
	0.3882	0.1933	0.0000
$Re = 708$	0.3673	-0.0041	0.0000
	0.3709	-0.0044	0.4952
	0.3745	0.0009	0.0000
	0.3781	-0.0022	0.4954
	0.3817	0.0001	0.0000
	0.3853	-0.0058	0.4954
	0.3888	-0.0064	0.0000
$Re = 700$	0.3654	-0.0438	0.0000
	0.3691	-0.0438	0.4947
	0.3727	-0.0374	0.0000
	0.3763	-0.0401	0.4948
	0.3800	-0.0367	0.0000
	0.3836	-0.0423	0.4948
	0.3872	-0.0419	0.0000

TABLE 3. Location of cusps, as determined via the faster approach, whereby all cusps are assumed to be matched to $\alpha \in \mathbb{R}$, i.e. $\alpha_i = 0$. Calculations for $Re = 750$ are in excellent agreement with results presented in table 2 that were based on the slower approach for locating cusps, i.e. wavenumbers α were allowed to be complex. Cusp locations are indicated by circular and diamond markers in figures 10 and 12.

harmonic and subharmonic modes marked in figure 10(a) and tabulated in tables 2 and 3. Although the leading-order behaviour, for large time τ, is governed by the single least stable mode, we do not expect this mode to dominate over a finite time period, as the harmonic and subharmonic modes develop with growth rates μ_r of commensurate size. Thus, for small time τ pointwise growth is described by a linear superposition of the multiple harmonic and subharmonic absolutely unstable modes. Since the superposition of harmonic and subharmonic modes is itself subharmonic, pointwise growth of the linear disturbance is subharmonic. This behaviour is consistent with the DNS computations presented in Ramage *et al.* (2020) for the spatiotemporal disturbance development; during at least the first 10-20 periods of wall motion the disturbance amplitude, about fixed spatial x-locations, grows every two cycles of wall motion. In their study, Ramage *et al.* (2020) found that subharmonic pointwise growth was brought about by the coalescence of two distinct wavepackets, the mother and granddaughter, in the spatiotemporal plane.

The harmonic modes depicted in figure 10 coincide with the local maxima of the Floquet growth rates μ_r. In particular, the most unstable of these harmonic modes lies on the global maximum that characterises the growth of the disturbance maximum (recall table 1). Thus, the pointwise growth of the disturbance, for large time τ, is equal to the growth of the disturbance maximum. This particular observation is a key result from the earlier DNS investigation by Ramage *et al.* (2020) (see figure 5 of their paper). Although such behaviour might be expected of a flow with no distinct upstream/downstream directions, it may appear somewhat at odds with the DNS computations reported in
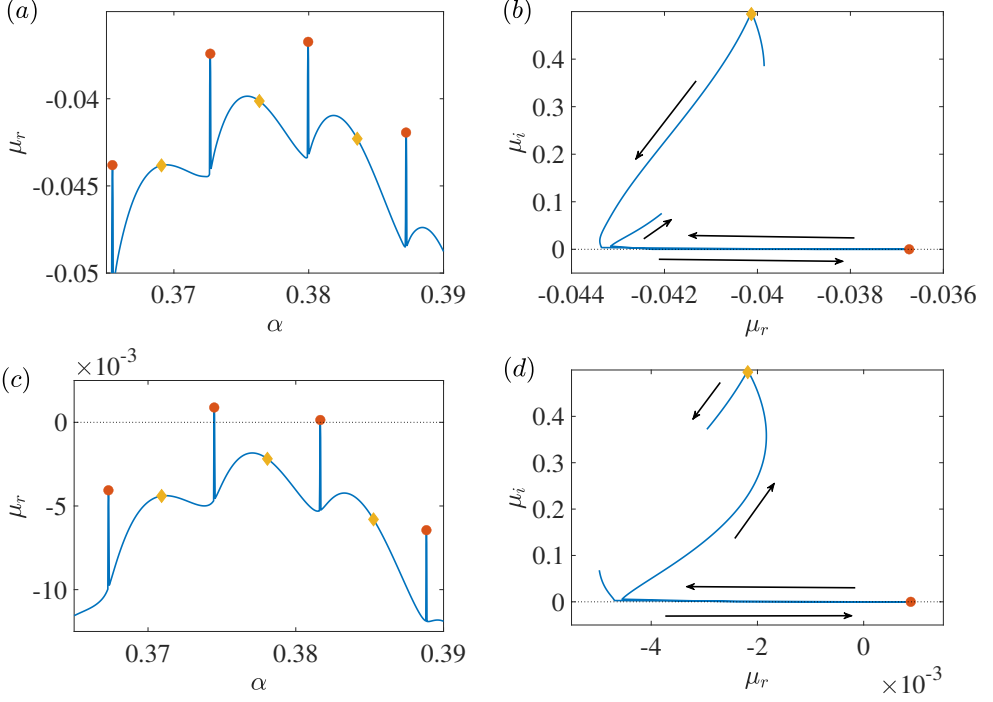
FIGURE 12. Equivalent to figure 10 but for (*a*, *b*) $Re = 700$ and (*c*, *d*) $Re = 708$. Floquet growth-rate μ_r as a function of the real wavenumber α in (*a*, *c*). Paths of the most unstable Floquet modes μ in the complex μ-plane in (*b*, *d*). Arrows indicate direction of increasing α. Red circular and yellow diamond markers indicate those locations matched to harmonic ($\mu_i = 0$) and subharmonic modes ($\mu_i = 1/2$), respectively.

Thomas *et al.* (2014). In their study, that was limited to the first three periods of wall motion, Thomas and co-workers observed asymmetric behaviour that favoured the direction dictated by the time at which the impulsive forcing was applied. However, the longer time simulations generated by Ramage *et al.* (2020) revealed that eventually the disturbance develops in a manner such that the pointwise growth is equivalent to that along the disturbance maximum.

Having shown that absolutely unstable behaviour arises for the Reynolds number $Re = 750$, and that cusp locations of the dispersion relation $D(\alpha, \mu) = 0$ are consistent with the DNS results of Ramage *et al.* (2020), we undertake an equivalent study for $Re = 700$ and $Re = 708$. The former case, $Re = 700$, is matched to a disturbance that is linearly stable for all wavenumbers α, as demonstrated by the negative valued Floquet growth rates μ_r in figure 8(*a*). In figure 12(*a*), the growth-rate μ_r is plotted over a reduced range of α, near the local maximum growth-rate (cross marker in figure 8(*a*)). Once again the Floquet growth-rate μ_r is characterised by regular finger-like protrusions, with harmonic cusps ($\mu_i = 0$) located at the tips of each finger and subharmonic cusps ($\mu_i = 0.5$) located about the mid-point between adjacent fingers. All cusps were located using the faster approach, whereby Floquet growth rates were traced in the complex μ-plane for real-valued α, as demonstrated in figure 12(*b*) for the least-stable cusps (both harmonic and subharmonic) and reported in table 3.

Unsurprisingly, all modes contributing to the pointwise development of the disturbance at $Re = 700$ are stable, i.e. $\mu_i < 0$. However, since the behaviour is analogous to that

described above for the Reynolds number $Re = 750$, we note that: pointwise evolution is dictated by a superposition of harmonic and subharmonic modes with comparable growth rates μ_r. Thus, initially, the pointwise development is subharmonic. Additionally, the location of the least-stable cusp is matched to the local maximum that dictates the growth of the disturbance maximum. Hence, the pointwise growth and the growth along the disturbance maximum are identical. These observations are again consistent with the disturbance characteristics reported in Ramage *et al.* (2020).

Given the above observations for both a strongly unstable ($Re = 750$) and stable disturbance ($Re = 700$), where the pointwise growth is found to be equal to the growth along the disturbance maximum, it would be natural to assume that the onset of instability coincides with the onset of absolutely unstable behaviour. In order to demonstrate the veracity of this conjecture we consider the disturbance established for the marginally unstable Reynolds number $Re = 708$. In figure 12(*c*), a small section of the Floquet growth-rate μ_r curve is plotted, with two unstable harmonic modes found about the tips of two protruding fingers (marked by red circles). These particular modes are matched to those finger-like protrusions found along the neutral stability curve in figure 6(*b*). As before, cusp locations and their stability characteristics were determined by tracing Floquet modes in the complex μ-plane for real wavenumbers α; demonstrated in figure 12(*d*) for the most unstable mode, with cusp locations tabulated in table 3. The pointwise evolution is governed by two marginally unstable harmonic modes and several marginally stable harmonic and subharmonic modes. Thus, the initial pointwise evolution of the impulse response will again be subharmonic. Moreover, pointwise growth about fixed spatial locations is again equal to that found along the disturbance maximum; the local maximum growth-rate μ_r is again found about the tip of a finger-like protrusion. Hence, the disturbance, for the marginally unstable Reynolds number $Re = 708$, is absolutely unstable.

5.3. *Spatial periodicity due to multiple absolutely unstable modes*

At fixed streamwise x-locations, the finite-time impulse response is a superposition of harmonic and subharmonic modes that satisfy the collision criteria. All such modes reported in table 3, for each given Reynolds number Re, are evenly spaced with respect to the wavenumber α. This then imposes a spatial periodicity on the solution, which suggests that the spacing between absolutely unstable modes is related to the fixed spatial spacing observed numerically between distinct wavepackets of the family-tree formation (recall figure 1 and the observations of Thomas *et al.* 2014; Ramage *et al.* 2020). Using DNS, Ramage *et al.* (2020) determined that the spatial spacing Λ between neighbouring (mother and daughter) wavepackets was governed by the Reynolds number Re (see figure 2 of the aforementioned paper). Furthermore, Ramage and co-workers observed a staggered wavepacket pattern in the family-tree structure, whereby a 2Λ spatial periodicity develops between wavepackets of comparable magnitude (see figures 3 and 4 of their paper, the former reproduced here in figure 1).

The relationship between the spatial periodicity Λ of individual wavepackets (as determined via DNS) and the wavenumber spacing between harmonic/subharmonic modes is investigated here by measuring the latter for a range of Reynolds numbers Re. These measurements are then compared with the Λ calculations presented by Ramage *et al.* (2020). Given the above observations for $Re = 700$, 708 and 750, we assume that all harmonic/subharmonic modes are evenly spaced along the wavenumber α-axis. Moreover, each mode alternates between harmonic behaviour at the finger tips and subharmonic behaviour at the mid-point between adjacent fingers. The wavenumber spacing $\Delta\alpha^f$ between finger protrusions is then readily computed for each Reynolds
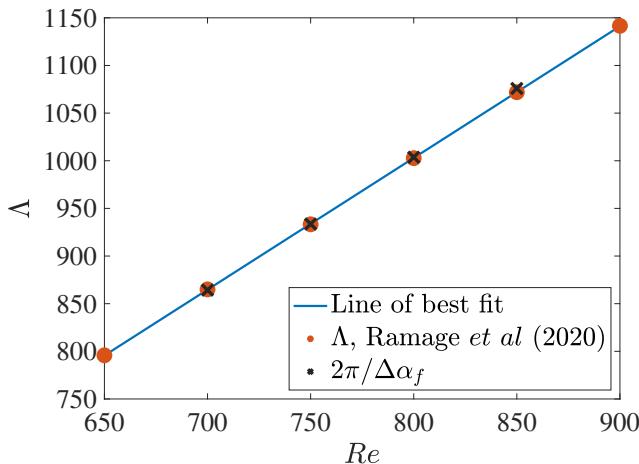
FIGURE 13. Spatial distance Λ between neighbouring wavepackets of the family-tree formation, as reported in Ramage *et al.* (2020) (circle markers), and spatial distance $2\pi/\Delta\alpha^f$ (cross markers) determined from the wavenumber distance $\Delta\alpha^f$ between finger-like protrusions along the real wavenumber α-axis.

number Re, without the construction of the numerically expensive cusp diagrams or the significant numerical resolution required to observe the cusp behaviour in the complex μ-plane. The distance between harmonic and subharmonic modes is then assumed to be half the distance between two adjacent fingers: $\Delta\alpha^f/2$. Since the evolution at fixed spatial locations consists of a discrete set of evenly-spaced modes, we anticipate a spatial periodicity of $4\pi/\Delta\alpha^f$ between wavepackets of comparable magnitude. Thus, given the observation by Ramage *et al.* (2020) that wavepackets of similar size are separated by a streamwise distance 2Λ, the following relationship between Λ and $\Delta\alpha^f$ is formulated

$$2\Lambda = \frac{4\pi}{\Delta\alpha^f} \Rightarrow \Lambda = \frac{2\pi}{\Delta\alpha^f}. \tag{5.1}$$

Hence, the streamwise distance Λ between each distinct wavepacket of the family-tree structure (i.e. between mother and daughter) is determined by the periodicity of the harmonic modes found at the tip of the finger-like protrusions.

The wavenumber spacing $\Delta\alpha^f$ between neighbouring finger protrusions is computed for several Reynolds numbers Re, and in each instance, $\Delta\alpha^f$ is found to be constant. Black cross markers in figure 13 depict the corresponding spatial distance $2\pi/\Delta\alpha^f$ as a function of Re, with the equivalent wavepacket spacing Λ (determined using DNS by Ramage *et al.* 2020) plotted using red circles. The solid blue line depicts the line of best fit. Excellent agreement is achieved between the two independent calculations for all cases considered. A small difference, equivalent to 0.2% of Λ, emerges for the Reynolds numbers $Re \geqslant 800$. However, this minor discrepancy is due to the approach in approximating $\Delta\alpha^f$ for these larger valued Reynolds numbers.

5.4. *Discussion*

Results presented in figures 9-12 and tables 2-3 suggest that there is a numerical inconsistency between where we expect the subharmonic cusps to occur and where they actually appear. The symmetry constraints, presented in §4.3, indicate that subharmonic cusps correspond to $\mu_i = 0.5$. However, the above cusp analysis found them at a marginally smaller value near $\mu_i = 0.497$. In an attempt to address this particular issue,

the least stable subharmonic cusp, for the Reynolds number $Re = 750$, was reproduced with an increasingly finer numerical resolution, with convergence to $\mu_i = 0.5$ anticipated. However, reducing the step size $\Delta\alpha$ by several orders of magnitude had a negligible effect on those Floquet growth rates μ_i reported in tables 2 and 3. Further validation checks were carried out for both larger harmonics N and the number of Chebyshev points along the wall-normal y-direction, but the cusp analysis remained unchanged. (Note that the corresponding harmonic cusps were always found for $\mu_i = 0$, below any numerical tolerance.)

While this apparent inconsistency remains largely unexplained, it is important to emphasise that the location of these subharmonic cusps is consistent with the disturbance development reported by Ramage *et al.* (2020). Hence, these cusps satisfy the collision criteria and are associated with the development of absolutely unstable behaviour.

6. Conclusions

The classification of linearly unstable behaviour in the time-periodic Stokes layer, as being convective or absolute, has been investigated using a modified form of the Briggs (1964) method. The approach used herein was adapted from that implemented by Brevdo & Bridges (1997) for temporally oscillating flows, with Floquet theory utilised to account for the periodicity of the flow. Given the antiperiodicity of the Stokes layer (2.2), symmetry constraints were derived that establish conditions for classifying linear disturbances as either convectively unstable or absolutely unstable. It was determined that the impulse response and pointwise development of the linear disturbances was dominated by those collisions that arose for wavenumbers $\alpha \in \mathbb{R}$ and Floquet exponents $\mu = \mu_r + ik/2$, with $k = 0$ and $k = 1$. Harmonic and subharmonic behaviour was then matched to those modes with $k = 0$ and $k = 1$, respectively.

Symmetry arguments were coupled to the cusp map method, developed by Kupfer *et al.* (1987), and used to locate absolutely unstable modes in the Stokes layer when the streamwise wavenumber $\alpha \in \mathbb{C}$. The analysis was applied to the unstable disturbance that develops for the Reynolds number $Re = 750$, with 6 cusps located in the complex Floquet exponent μ-plane. In each instance, the wavenumber α was real-valued only. Three of these cusps were found about the tips of fingers that protrude from the growth-rate curves and correspond to $\mu_i = 0$, i.e. stationary waves. The remaining three cusps were located about the mid-point between adjacent fingers, with $\mu_i \approx 1/2$. Thus, cusp locations were matched to both harmonic and subharmonic behaviour. Hence, the pointwise growth of linear disturbances is characterised by subharmonic behaviour, which is consistent with the DNS computations presented by Ramage *et al.* (2020); about fixed streamwise positions, the disturbance grows every two full periods of wall oscillation. Moreover, as the real part of the Floquet exponent μ was positive for each of these 6 cusps, the linear disturbance for $Re = 750$ is classified as absolutely unstable.

Cusps in the complex μ-plane were only found for real-valued streamwise wavenumbers α. The analysis was therefore extended to the respective stable and marginally unstable Reynolds numbers $Re = 700$ and $Re = 708$, with $\alpha \in \mathbb{R}$. Thus, the significant computational requirements in generating cusp map diagrams was no longer necessary. As with the larger valued Reynolds number ($Re = 750$), linear disturbances were again characterised by both harmonic and subharmonic modes. Furthermore, it was demonstrated that the Floquet mode with the largest growth-rate, that dictates the growth of the disturbance maximum, coincides with the mode that dictates the pointwise growth of the disturbance. Thus, the growth-rate about fixed spatial locations is identical to the growth-rate of the disturbance maximum, which is consistent with the earlier DNS observations of Ramage

et al. (2020): the onset of linear instability in the Stokes layer, with the critical Reynolds number $Re_c = 707.84$ (as first observed by Blennerhassett & Bassom 2002), coincides with the onset of absolutely unstable behaviour.

Finally, it was shown that the spatial periodicity imposed by the regular spacing of cusps with respect to the wavenumber α is consistent with the periodic spatial spacing between wavepackets of the family-tree structure simulated numerically by Ramage *et al.* (2020).

Future work

Following the earlier studies by Thomas *et al.* (2015) and Ramage *et al.* (2020), a natural next step would be to extend the analysis to the family of flows established when the wall motion is modified via a low-amplitude, high-frequency noise. This family of flows would be of particular interest because, depending on the harmonic frequency of the noise-like modulation, it is possible to construct a flow that is not antiperiodic. In fact, it was reported by Ramage *et al.* (2020) that for these non-antiperiodic flows, the pointwise growth-rate is no longer equal to the growth-rate of the disturbance maximum. Moreover, the disturbance develops a spatially asymmetric structure, while still exhibiting pointwise growth. The present framework would provide a solid theoretical foundation for these flows and for the reported breakdown of the family-tree structure, so long as a suitable method for testing the collision criteria is introduced for cases where the symmetry arguments are no longer valid (some preliminary results are outlined in Ramage 2017).

Acknowledgements

Declaration of interest

The authors report no conflict of interest.

REFERENCES

AKHAVEN, R., KAMM, R. D. & SHAPIRO, A. H. 1991 An investigation of transition to turbulence in bounded oscillatory flows. Part 1. Experiments. *J. Fluid Mech.* **225**, 395–422.

BLENNERHASSETT, P. J. & BASSOM, A. P. 2002 The linear stability of flat Stokes layers. *J. Fluid Mech.* **464**, 393–410.

BLENNERHASSETT, P. J. & BASSOM, A. P. 2006 The linear stability of high-frequency oscillatory flow in a channel. *J. Fluid Mech.* **556**, 1–25.

BREVDO, L. & BRIDGES, T. J. 1996 Absolute and convective instabilities of spatially periodic flows. *Philos. Trans. Royal Soc. A* **354**, 1027–1064.

BREVDO, L. & BRIDGES, T. J. 1997 Absolute and convective instabilities of temporally oscillating flows. *Z Angew Math Phys* **48**, 290–309.

BRIGGS, R. J. 1964 *Electron-stream interaction with plasmas.* MIT Press.

CLAMEN, M. & MINTON, P. 1977 An experimental investigation of flow in an oscillating pipe. *J. Fluid Mech.* **81**, 421–431.

CONRAD, P. W. & CRIMINALE, W. O. 1965 The stability of time-dependent laminar flow: Parallel flows. *Z Angew Math Phys* **16**, 233–254.

ECKMANN, D. M. & GROTBERG, J. B. 1991 Experiments on transition to turbulence in oscillatory pipe flow. *J. Fluid Mech.* **222**, 329–350.

GASTER, M. 1968 Growth of disturbances in both space and time. *Phys. Fluids* **11**, 723–727.

HALL, P. 1978 The linear stability of flat Stokes layers. *Proc. Royal Soc. A* **359**, 151–166.

HINO, M., SAWAMOTO, M. & TAKASU, S. 1976 Experiments on transition to turbulence in an oscillatory pipe flow. *J. Fluid Mech.* **75**, 193–207.

HUERRE, P. 2002 Open shear flow instabilities. In *Perspectives in Fluid Dynamics* (ed. M. G. Worster G. K. Batchelor, H. K. Moffatt), chap. 4, pp. 159–229. Cambridge University Press.

HWANG, Y., KIM, J. & CHOI, H. 2013 Stabilization of absolute instability in spanwise wavy two-dimensional wakes. *J. Fluid Mech.* **727**, 346–378.

KUPFER, K., BERS, A. & RAM, A. K. 1987 The cusp map in the complex-frequency plane for absolute instabilities. *Phys. Fluids* **30**, 3075–3082.

LINGWOOD, R. J. 1995 Absolute instability of the boundary layer on a rotating disk. *J. Fluid Mech.* **299**, 17–33.

LINGWOOD, R. J. 1997 On the applications of the Briggs' and steepest-descent methods to a boundary-layer flow. *Stud Appl Math* **98**, 213–254.

LINGWOOD, R. J. 1997 On the effects of suction and injection on the absolute instability of the rotating-disk boundary layer. *Phys. Fluids* **9**, 1317–1328.

PIER, B. 2003 Finite-amplitude crossflow vortices, secondary instability and transition in the rotating-disk boundary layer. *J. Fluid Mech.* **487**, 315–343.

RAMAGE, A. 2017 Linear disturbance evolution in the semi-infinite Stokes layer and related flows. PhD thesis, School of Mathematics, Cardiff University.

RAMAGE, A., DAVIES, C., THOMAS, C. & TOGNERI, M. 2020 Numerical simulation of the spatio-temporal development of linear disturbances in Stokes layers: Absolute instability and the effects of high frequency harmonics. *Phys. Rev. Fluids* **5**, 103901.

SCHMID, P. J. & HENNINGSON, D. S. 2001 *Stability and transition in shear flows.* Springer-Verlag, New York.

THOMAS, C. 2020 The linear stability of an acceleration-skewed oscillatory stokes layer. *J. Fluid Mech.* **895**, A27.

THOMAS, C. 2021 Effects of velocity skewness on the linear stability of the oscillatory stokes layer. *Phys. Fluids* **33**, 034104.

THOMAS, C., BASSOM, A. P. & BLENNERHASSETT, P. J. 2012 The linear stability of oscillating pipe flow. *Phys. Fluids* **24**, 014106.

THOMAS, C., BASSOM, A. P., BLENNERHASSETT, P. J. & DAVIES, C. 2011 The linear stability of oscillatory Poiseuille flow in channels and pipes. *Proc. Royal Soc. A* **467**, 2643–2662.

THOMAS, C., BLENNERHASSETT, P. J., BASSOM, A. P. & DAVIES, C. 2015 The linear stability of a Stokes layer subjected to high frequency perturbations. *J. Fluid Mech.* **764**, 193–218.

THOMAS, C., DAVIES, C., BASSOM, A. P. & BLENNERHASSETT, P. J. 2014 Evolution of disturbance wavepackets in an oscillatory stokes layer. *J. Fluid Mech.* **752**, 543–571.

TREFETHEN, L. N. 2000 *Spectral methods in MATLAB.* Society for Industrial and Applied Mathematics.

VON KERCZEK, C. & DAVIS, S. H. 1974 Linear stability theory of oscillatory Stokes layers. *J. Fluid Mech.* **62**, 753–773.